A Quantitative Multi-Scale Analysis for Revealing Site-Proximity Effects in Tandem Catalysis

Fatima Mahnaz,[a] Ashfaq Iftakher,[a] M G Toufik Ahmed,[a] Aojie Li,[b] Jenna Vito,[a] Jasan Mangalindan,[a] Andrew Iovine,[a] M. M. Faruque Hasan,[a,c] Srinivas Rangarajan,[b] and Manish Shetty*[a]

[a] Artie McFerrin Department of Chemical Engineering, Texas A&M University
100 Spence Street, College Station, TX-77843. USA.
E-mail: manish.shetty@tamu.edu
[b] Texas A&M Energy Institute
617 Research Parkway, College Station, TX-77843-3372.
[c] Chemical and Biomolecular Engineering, Lehigh University
HST Building, L136 124 E. Morton Street, Bethlehem, PA 18015. USA.

S1. Materials and chemicals

Zinc nitrate hexahydrate ($Zn(NO_3)_2.6H_2O$, ≥ 99%, Sigma Aldrich, US) and zirconium (IV) oxynitrate hydrate (≥ 99.5%, thermoscientific, US) were used to synthesize zinc-zirconium oxide ($ZnZrO_x$).
Aluminum nitrate hydrate (99.999% Beantown Chemicals, US), tetrapropylammonium hydroxide (TPAOH, 40 wt/wt % in H_2O, Beantown Chemicals, US), tetrapropylammonium bromide (TPABr, 98+%, Alfa Aesar, US), ammonium hydroxide (NH_4OH, Certified ACS Plus, Fisher Chemical, US), sodium aluminate ($NaAlO_2$, technical grade, Beantown Chemicals, US), sodium chloride (NaCl, Macron, ACS grade), tetraethyl orthosilicate (TEOS, Aldrich, 98%), sodium hydroxide (NaOH, 97%, Sigma Aldrich, US), silica sol (LUDOX, AS-40, 40 wt%, Sigma Aldrich, US), sulfuric acid (99%, Sigma Aldrich, US) were used to synthesize MFI zeolites with different crystal sizes.
Zeolite Socony Mobil–5 (NH_4-ZSM-5, CBV 8014, Si:Al ratio 40) zeolite was purchased from Zeolyst (Kansas City, US).
Fused α-Alumina (100-200 mesh, Sigma Aldrich, US) was used for spacing in stacked bed catalysts.
Methanol (ACS grade, Sigma Aldrich, US) was used for methanol-to-hydrocarbon (MTH) conversion reactions.

S2. Physisorption analysis

Surface area measurements were performed using the Anton Paar Autosorb iQ-C-MP EPDM automated gas sorption analyzer. The surface area analysis was carried out using nitrogen physisorption at 87 K, and the resulting adsorption-desorption isotherms were analyzed using the Brunauer-Emmett-Teller (BET) theory [1]. In summary, a quantity of 10-15 mg of the catalyst was placed in a 6 mm glass cell bulb (without a rod) or a 9 mm glass cell with a rod to reduce void volume. The sample underwent an initial outgassing process at 350°C for 480 min. Nitrogen physisorption isotherm data were then collected, encompassing 72 adsorption (p/p_o values of $1e^{-6}$ to 0.995) and 27 desorption points (p/p_o values of 0.05 to 0.995). The isotherm data were subjected to BET analysis, specifically utilizing the adsorption data points ranging from p/p_o values of 0.005 to 0.3. Total pore volume was calculated based on the assumption that at relative pressures near unity, the pores filled with liquid following the equation below [2]:

$$V_{liq} = \frac{P_a V_{ads} V_m}{RT} \quad \text{(S1)}$$

The micropore area and volume were calculated using the t-plot method using the deBoer thickness equation (see below) using adsorption data points ranging from p/p_o values of 0.2 to 0.5. All zeolite-containing samples contained a positive y-intercept on the t-plot indicating the presence of micropores, whereas the bulk ZnZrO sample t-plot passed through the origin confirming their mesoporous identity.

$$t = \left[\frac{13.99}{\log(P_0/P)+0.034}\right]^{\frac{1}{2}} \quad \text{(S2)}$$

The t-plot is a graph of the volume of gas adsorbed at STP (V_{ads}^{STP}) vs the layer thickness (t). The slope of this line (s) is related to the total surface area of the pores given by the equation below. It then follows that the micropore surface area (S_{MP}) is the difference between the BET surface area and S_t.

$$S_t\ (m^2/g) = \frac{V_{ads}^{STP} \times 15.47}{t} = s \times 15.47 \quad \text{(S3)}$$

$$S_{MP} = S_{BET} - S_t \quad \text{(S4)}$$

For samples without micropores, there is good agreement between S_{BET} and S_t (such is the case for bulk ZnZrO). The micropore volume is related to the intercept (i) of this plot given by the following equation.

$$V_{MP} = i \times 0.001547\ (cm^3) \quad \text{(S5)}$$

Details on BET calculation parameters (slope and intercept) and micropore volume calculations are given in **Table S6**.

S3. Mass transport analysis for CH_3OH synthesis

S3.1. Mears criterion for external diffusion

Mears' criterion was estimated to establish the absence of any external mass-transfer limitations.[3]

$$\frac{-r_{(obs)} \times \rho_b \times R \times n}{k_c \times C_b} < 0.15 \qquad \text{(S6)}$$

where $-r_{(obs)}$ is the observed reaction rate for the conversion of CO_2 to CH_3OH in mole kg $cat^{-1}s^{-1}$, ρ_b is the catalyst bed density in kg m^{-3}, R is the catalyst pellet size in m, n is the reaction order, k_c is the mass-transfer coefficient in m s^{-1}, and C_b is the bulk feed gas concentration at a reaction temperature of 623 K, in mol m^{-3}. The Reynolds number of the flow around the catalyst pellet is given by $Re = 2\mathrm{U} \times \mathrm{R} \times \rho/\mu$, where U is the superficial velocity in m s^{-1}, R is the catalyst pellet radius in m, ρ is the density in kg m^{-3}, and μ is the viscosity in kg m^{-1} s^{-1}, of the reactant mixture. The mass-transfer coefficient can be estimated using the Sherwood number ($Sh = k_c \times \frac{2\mathrm{R}}{\mathrm{D}} = 2$) since Reynolds number is found to be far less than 1, where D is the diffusivity of the reactant (CO_2 and H_2) mixture in m^2 s^{-1}. **Table S1** tabulates all the relevant parameters. We assumed the order of reaction is $n = 1$, to over-estimate the left side of the inequality in Eq. S6. If the criterion is satisfied for $n = 1$, it is likely to be satisfied for any fractional-order reaction. As seen in **Table S1**, the absence of external mass-transfer limitations is confirmed by Mears' criterion ($1.9 \times 10^{-3} << 0.15$).

Table S1: Values of parameters relevant to the calculation of Mears' criterion for estimating the external mass-transfer limitation.

Parameters relevant for estimation of Mears' criterion	Values
Observed reaction rate: $-r_{(obs)}$(mole g_{cat}^{-1} s^{-1})	8.43×10^{-6}
Catalyst bed density: ρ_b (g cm^{-3})[a]	1.9
Pellet radius: R (m)	2.1×10^{-8}
Reaction order: n[b]	1
Bulk concentration: C_b(g cm^{-3})[c]	8×10^{-3}
Superficial velocity: U (m s^{-1})	5.3×10^{-2}
Viscosity: μ (g cm^{-1} s^{-1})[d]	1.4×10^{-5}
Fluid density: ρ (kg m^{-3})[d]	8.3×10^{-3}
Reynold's number: *Re*	1.2×10^{-1}
Diffusion coefficient: *D* (cm^2 s^{-1})[e]	2.3×10^{-2}
Mass-transfer coefficient: k_c (cm s^{-1})[f]	1.075
Mears' criterion	1.9×10^{-3}

a: Catalyst bed density estimated by measuring the mass of catalyst pellets packed into a known cylindrical volume.
b: Reaction order considered as 1 for this calculation to obtain an upper limit on the Mears' criterion.
c: Bulk concentration calculated from ideal gas.

d: Viscosity taken for H_2 gas, and fluid density calculated from the ideal gas law, at 623 K.
e: Diffusion coefficient calculated for CO_2-H_2 mixture at 623 K. Critical point taken as (33.2 K, 12.95 atm), and (304.2 K, 72.0 atm) for H_2, and CO_2, respectively.[4]
f: k_c calculated from the relation $Sh = k_c \times \frac{2R}{D} = 2$. $k_c = \frac{D}{R}$

S3.2. Weisz–Prater criterion for internal diffusion
The absence of internal mass-transfer limitations was estimated using the Weisz-Prater criterion (Eq. S7).[3]

$$C_{WP} = \frac{-r_{(obs)} \times \rho_c \times R^2}{D_e \times C_s} \ll 1 \qquad \text{(S7)}$$

where $-r_{(obs)}$ is the observed reaction rate for the conversion of CO_2 to CH_3OH in mole kg cat^{-1}s^{-1}, ρ_c is the catalyst density in kg m^{-3}, R is the catalyst pellet radius in m, D_e is the effective diffusivity in m^2 s^{-1}, and C_s is the surface concentration of CO_2 and H_2 at a reaction temperature at 623 K, in mol m^{-3}. C_{WP} is found to be 0.054 $\ll$ 0.01. If $C_{WP} \ll 1$, the reaction is not internal mass-transfer limiting. Note that the effective diffusivity is considered a combination of Knudsen and molecular diffusivities, denoted by D_T, estimated from the Bosanquet equation.[5]

Table S2: Values of parameters relevant to the calculation of the Weisz-Prater criterion for estimating the internal mass-transfer limitation.

Parameters relevant for Weisz-Prater criterion	Values
Observed reaction rate: $-r_{(obs)}$(mole g_{cat}^{-1} s^{-1})	8.4×10^{-6}
Catalyst density: ρ_b (g cm^{-3})[a]	1.9
Pellet radius: R (m)	2.1×10^{-8}
Knudsen diffusivity: D_K (cm^2 s^{-1})	8.7×10^{-3}
Effective molecular diffusivity: D_{eM} (cm^2 s^{-1})[b]	2.3×10^{-2}
Transition diffusivity: D_T (cm^2 s^{-1})[c]	2.5×10^{-3}
Surface concentration: C_s(mol cm^{-3})[d]	1.66×10^{-4}
C_{WP}[e]	0.054

a: Density is taken as the catalyst packing density.
b: Effective molecular diffusivity $D_{eM} = \frac{D_M \times \phi}{\tau}$. In the absence of experimental values, porosity ϕ and tortuosity (τ), values are taken as 0.35 and 2.0, respectively.[6,7]
c: Transition diffusivity is calculated from Bosanquet equation.[5]
d: In the absence of external mass-transfer limitation, surface concentration is the same as bulk concentration.
e: Transition diffusivity is used in the estimation of C_{WP}.

S3.3. Analysis for Peclet number

Diffusivity (D) calculation

The diffusion coefficient was calculated for CO_2-H_2 mixture at 623 K and 500 psig, using the empirical correlation developed by Fuller.[8]

$$D_{CH3OH-CO2\ \&\ H2} = \frac{10^{-3} T^{1.75} \left(\frac{1}{M_A} + \frac{1}{M_B}\right)^{0.5}}{P \left((\sum V_A)^{\frac{1}{3}} + (\sum V_B)^{\frac{1}{3}} \right)^2}$$

Where P represents total pressure, atm; M_i = molecular weight; $D_{CH3OH\text{-}CO2\&H2}$ = diffusivity, cm^2s^{-1}; T = temperature, K; $\sum V_i$ = Sum of the diffusion volume for a specific molecule.

Péclet (Pe) number calculation

The Péclet number serves as an indicator of the relative influence of advection in comparison to diffusion.[4,9] A high Péclet number signifies the prevalence of advection in the flow, while a low Péclet number indicates the dominance of diffusion. If we analyze advection and diffusion using characteristic time scales, the Péclet number represents the ratio between these time scales. The determination of these time scales is based on dimensional constraints.

The time scale for advection, denoted as T_A, is approximately equal to the ratio of the characteristic length scale, L, to the flow speed, v:

Advection time scale ≈ $T_A \sim L/v$

Likewise, the time scale for diffusion, denoted as T_D, is approximately equal to the ratio of the square of the characteristic length, L^2, to the diffusivity, D:

Diffusion time scale ≈ $T_D \sim L^2/D$

Consequently, the Péclet number can be expressed as the ratio of the diffusion time scale to the advection time scale:

$Pe = T_D / T_A = vL/D$

When $T_A << T_D$ transport by advection is faster than transport by diffusion, and we say that the system is not advection limited. This corresponds to Pe >> 1 (vice versa for Pe << 1).

Table S3: Parameters of calculation of Pe number in the catalyst bed. Reaction conditions: 350 °C, 500 psig, H_2:CO_2 ratio 3:1, total flow 267 ml/min.

Parameters relevant for diffusivity	Values
Pressure (MPa)	3.44
Temperature (K)	623
Total feed flowrate (mL/min)	267
Linear velocity of feed, v (cm/s)[a]	0.573
Reactor diameter, (cm)	0.77
Catalyst bed length (cm)	2.54
Catalyst porosity, ε	0.39
Pellet diameter (cm)	0.042
Diffusion volume of H_2	7.07
Diffusion volume of CO_2	26.9
Diffusion volume of CH_3OH	30
MW of CH_3OH	32.0
MW of CO_2-H_2 feed	8.51
$D_{CH3OH-CO2\&H2}$ **(cm²/s)**	0.03
$D_{eff,CH3OH-CO2\&H2}$ **(cm²/s)**	0.006
$D_{CO2-CO2\&H2}$ **(cm²/s)**	0.02
$D_{eff,CO2-CO2\&H2}$ **(cm²/s)**	0.005
$D_{H2-CO2\&H2}$ **(cm²/s)**	0.09
$D_{eff,H2-CO2\&H2}$ **(cm²/s)**	0.023
Pe_{CO2}	201.21
Pe_{H2}	47.92
Pe_{CH3OH}	44.80

a: Linear velocity was calculated using ideal gas law.

The high Pe number (>40) for all components suggest that the system is not advection limited.

S4. Reaction network for CH_3OH synthesis and kinetic analysis

We considered two possible cases for CH_3OH synthesis network:

(i) methanol synthesis ($CO_2 + 3H_2 \rightarrow CH_3OH + H_2O$)

(ii) reverse water gas shift (RWGS) ($CO_2 + H_2 \rightarrow CO + H_2O$)

(iii) CO hydrogenation to CH_3OH ($CO + 2H_2 \rightarrow CH_3OH$) or CH_3OH decomposition to CO ($CH_3OH \rightarrow CO + 2H_2$).[10]

Case 1: Considering CO hydrogenation to methanol (CO-MS)

1. $\boldsymbol{CO_2 + 3H_2 \rightarrow CH_3OH + H_2O}$ (MS)
2. $\boldsymbol{CO_2 + H_2 \rightarrow CO + H_2O}$ (RWGS)
3. $\boldsymbol{CO + 2H_2 \rightarrow CH_3OH}$ (CO-MS)

Rate expressions:

- $r_{CH_3OH} = k_{MS}\, P_{CO_2} + k_{CO-MS}\, P_{CO}$
- $r_{CO} = k_{RWGS}\, P_{CO_2} - k_{CO-MS}\, P_{CO}$

Assuming, $P_{CO} \approx P_{CO_2}\, X_{CO_2} \frac{k_{RWGS}}{k_{MS}}$ at low X_{CO_2}

$$\frac{S_{CO}}{S_{CH_3OH}} = \frac{k_{RWGS}\, P_{CO_2} - k_{CO-MS}\, P_{CO}}{k_{MS}\, P_{CO_2} + k_{CO-MS}\, P_{CO}}$$

$$= \frac{k_{RWGS} - k_{CO-MS} \frac{k_{RWGS}}{k_{MS}} X_{CO_2}}{k_{MS} + k_{CO-MS} \frac{k_{RWGS}}{k_{MS}} X_{CO_2}}$$

$$\frac{S_{CO}}{S_{CH_3OH}} = \frac{k_{RWGS}}{k_{MS}} - \frac{k_{RWGS}\, k_{CO-MS}}{k_{MS}^2} X_{CO_2}$$

Therefore, plotting $\frac{S_{CO}}{S_{CH_3OH}}$ with respect to X_{CO_2} will yield a negative slope.

Case 2: Considering methanol decomposition to CO (MD)

Rate expressions:

- $r_{CH_3OH} = k_{MS}\, P_{CO_2} - k_{MD}\, P_{CH_3OH}$
- $r_{CO} = k_{RWGS}\, P_{CO_2} + k_{MD}\, P_{CH_3OH}$

$$\frac{S_{CO}}{S_{CH_3OH}} = \frac{k_{RWGS}\, P_{CO_2} + k_{MD}\, P_{CH_3OH}}{k_{MS}\, P_{CO_2} - k_{MD}\, P_{CH_3OH}}$$

$$= \frac{k_{RWGS} + k_{MD} \frac{k_{MS}}{k_{RWGS}} X_{CO_2}}{k_{MS} - k_{MD} \frac{k_{MS}}{k_{RWGS}} X_{CO_2}}$$

$$\frac{S_{CO}}{S_{CH_3OH}} = \frac{k_{RWGS}}{k_{MS}} + \frac{k_{MD}}{k_{RWGS}} X_{CO_2}$$

Therefore, plotting $\frac{S_{CO}}{S_{CH_3OH}}$ with respect to X_{CO_2} will yield a positive slope.

S5. Approach-to-equilibrium

S5.1. Calculations for approach-to-equilibrium

Reaction quotient Q (=$\frac{P_{CH_3OH,eff}\,P_{H_2O}P^{\circ 2}_{STD}}{P_{CO_2}P^{3}_{H_2}}$) for CH_3OH synthesis under tandem reaction conditions was calculated based on partial pressure of reactants and products (p_{CO_2}, p_{H_2}, $p_{CH_3OH,eff}$ and p_{H_2O}). It is to be noted that we calculated $p_{CH_3OH,eff}$ by assuming all hydrocarbons form *via* CH_3OH intermediate, therefore, $p_{CH_3OH,eff}$ = $p_{CH_3OH} + \sum p_{HC}$. Additionally, $p_{H_2}$and p_{H_2O} was calculated based on H-balance.

The equilibrium constant K_p was calculated from the Gibbs free energy represented as:

$$\frac{nG}{RT} = \sum n_i \left[\frac{\Delta_f G^o_{i,T}}{RT} + \ln\left(y_i P\right)\right] \quad \text{(S8)}$$

where n_i is the number of moles of component i, $\Delta_f G^o_{i,T}$ is the Gibbs free energy of formation of component i at temperature T, R is the universal gas constant, y_i is the mole fraction of component i, and P is the pressure.

The temperature-dependent Gibbs free energy was derived from the following equations:

$$\frac{d\left(\frac{\Delta_f G^o_i}{T}\right)}{dT} = \frac{\Delta_f H^o_i}{T^2} \quad \text{(S9)}$$

$$\Delta_f H^o_{i,T} = \Delta_f H^o_{i,T_R} + \int_{T_R}^{T} \Delta C_{p,i} dT \quad \text{(S10)}$$

$$\frac{C_{p,i}}{R} = A_i + B_i T + C_i T^2 + \frac{D_i}{T^2} \quad \text{(S11)}$$

where $\Delta_f H^o_{i,T}$ is the enthalpy of formation of component i at temperature T, $\Delta_f H^o_{i,T_R}$ is the enthalpy of formation of component i at a reference temperature T_R, and $C_{p,i}$ is the temperature-dependent heat capacity of component i. The values of A, B, C, and D were obtained from a chemical engineering textbook.[11]

Approach to equilibrium (*z*) was calculated as, *z* = $\frac{Q}{K_p}$.

Table S4: Approach-to-equilibrium (z) for CH_3OH synthesis under tandem reaction conditions reported in the literature.

Zeolite Type	Catalyst	Reaction Parameters			CO_2 conv (%)	CO sel (%)	z	Reference
		T (°C)	P (MPa)	GHSV ($mL/g_{cat}/h$)				
SAPO-34	$ZnZrO_x$/SAPO-34	380	2	3600	12.6	46.6	1.16	[12]
	In_2O_3-ZrO_2/SAPO-34	400	1.5	12000	15.7	87.6	0.78	[13]
	In_2O_3/SAPO-34	360	2.5	6000	28.7	81.1	1.10	[14]
	$ZnZrO_x$/SAPO-34	375	1	2100	17.9	72.7	1.06	[15]
	PdZn/ZrO_2+SAPO-34	350	5	12000	24.8	66.4	0.35	[16]
	$GaZrO_x$/H-SAPO-34	350	3	2400	18.9	44.1	1.01	[17]
	$ZnZrO_x$/SAPO-34	350	3	4000	17.3	28.4	0.69	[18]
	Mn-Zn-Zr/Zn-SAPO-34	340	2	5600	18.1	65.0	0.84	[19]
HZSM-5	In_2O_3/HZSM-5	340	3	9000	13.1	44.8	0.17	[13].
	ZnZrO/ZSM-5	320	4	1200	12.9	41.2	0.06	[20]
	ZnO-ZrO_2/HZSM-5	340	4	7200	15.9	34.3	0.14	[21]
	ZrZn/HZSM-5	350	3	12000	7.5	48.0	0.08	[22]
	$ZnZrO_x$/HZSM-5	315	3	1020	15.5	35.3	0.17	[23]
	$ZnZrO_x$/NZ5	320	3	4000	10.6	20.9	0.11	[24]
	In-$ZnZrO_x$/NZ5	320	3	4000	11.7	21.0	0.10	[24]
	In$ZnZrO_x$/NZ5	320	3	4000	13.8	19.8	0.14	[24]
	$ZnZrO_x$/NZ5-DS	320	3	4000	16.0	18.1	0.23	[25]
	In_2O_3-ZnZrOx/NZ5-DS	320	3	4000	22.4	11.0	0.59	[25]
	$ZnZrO_x$/ZSM-5	320	4	7200	7.2	27.9	0.25	[26]
SSZ-13	$InZrO_x$/SSZ-13	350	4	1000	24.2	61.2	0.57	[27]
	$GaZrO_x$/H-SSZ-13	350	3	2400	16.3	27.2	0.93	[17]

	$InZrO_x$/H-SSZ-13	350	3	2400	22.0	52.0	1.14	[17]
	$ZnZrO_x$/H-SSZ-13	350	3	2400	21.4	37.2	1.51	[17]
	In_2O_3/SSZ-13	400	3	6400	48.6	78.7	2.19	[28]
	$ZnZrO_x$/SSZ-13	360	1	4500	6.0	34.4	0.87	[29]
	$GaInO_3$/SSZ-13	362	2	5920	11.6	74.6	0.36	[30]
RUB-13	ZnZrOx/H-RUB-13	350	3	4000	15.3	28.2	0.73	[18]
	$ZnCrO_x$/H-RUB-13	350	3	4000	12.9	53.3	0.24	[18]
	$ZnAl_2O_x$/H-MOR	320	3	1500	17.0	60.0	0.26	[31]
	$ZnAl_2O_x$/Py-H-MOR	320	3	1500	16.0	70.0	0.21	[31]
ZSM-11	$GaZrO_x$/H-ZSM-11	350	3	2400	16.5	38.9	0.65	[17]
ZSM-35	$GaZrO_x$/H-ZSM-35	350	3	2400	17.8	48.3	0.91	[17]
MAPO-18	$ZnZrO_x$+MgAPO-18	375	3	12000	11.3	44.5	0.34	[32]
	$ZnZrO_x$+SAPO-18	375	3	12000	11.0	46.0	0.29	[32]

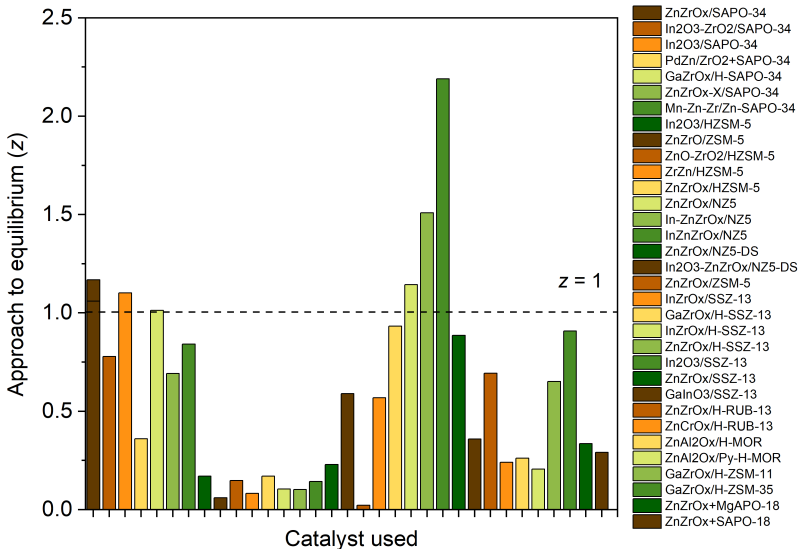

Fig. S1: Approach to equilibrium for CH_3OH synthesis under tandem reaction conditions reported in the literature.

S6. Kinetics studies on CH_3OH synthesis

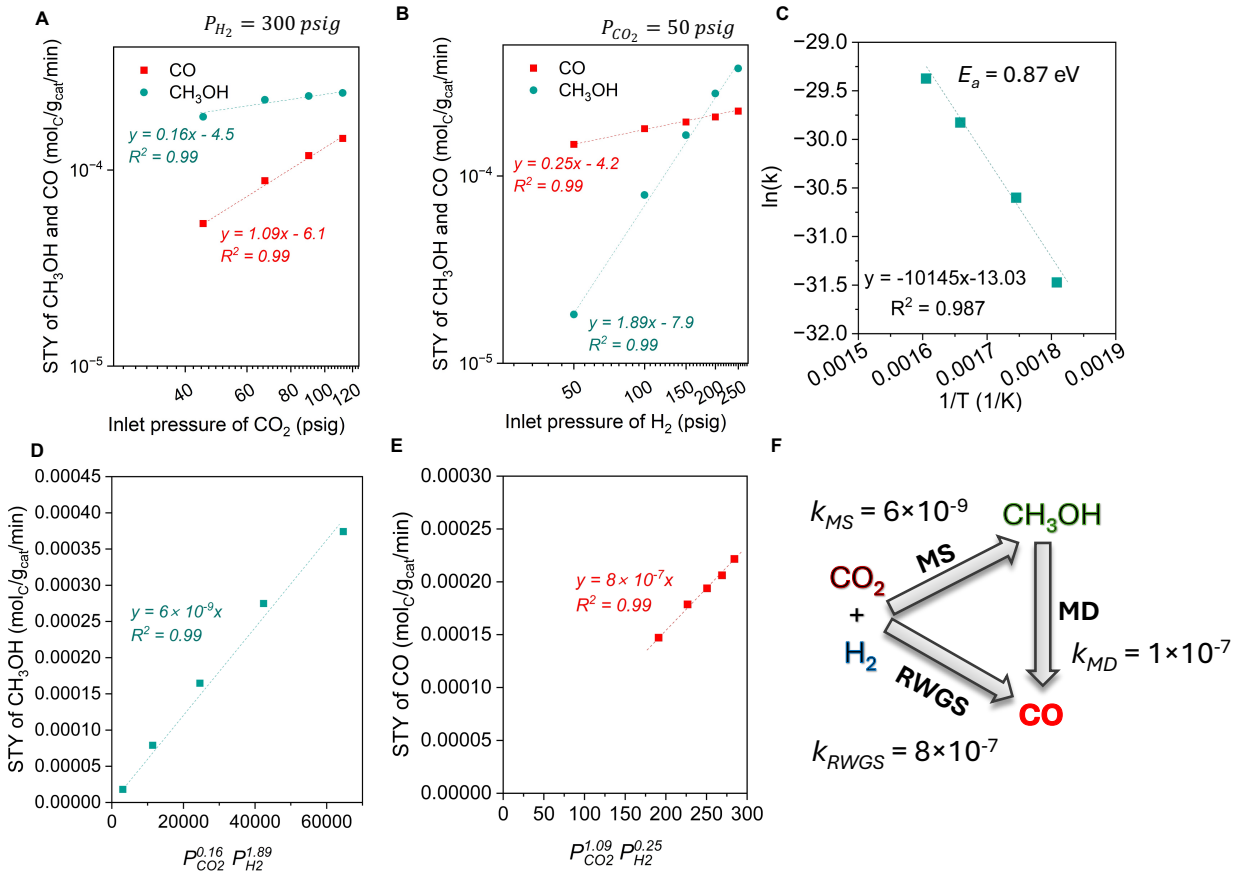

Fig. S2: A) Space-time yield of CH_3OH and CO at different partial pressures of CO_2 (p_{CO_2}) at constant p_{H_2}. Reaction conditions: 350 °C, 500 psig, total flow 280 ml/min, catalyst $ZnZrO_x$, mass 0.3 g, p_{H_2}=300 psig. Total pressure was kept constant using N_2 as an inert. The catalyst was pretreated in 5% H_2 (balance N_2) at 300°C for 1 h and cooled to 40 °C prior to the reaction. B) Space-time yield of CH_3OH and CO at different partial pressures of H_2 (p_{H_2}) at constant p_{CO_2}. Reaction conditions: 350 °C, 500 psig, total flow 280 ml/min, catalyst $ZnZrO_x$, mass 0.3 g, p_{CO_2}=50 psig. Total pressure was kept constant using N_2 as an inert. The catalyst was pretreated in 5% H_2 (balance N_2) at 300°C for 1 h and cooled to 40 °C prior to the reaction. C) Arrhenius plot at different reaction temperatures (280, 300, 330, and 350°C). The catalyst was pretreated in 5% H_2 (balance N_2) at 300°C for 1 h and cooled to 40 °C prior to the reaction. D) Finding the rate constant for CO_2 to CH_3OH formation. E) Finding the rate constant for CO_2 to CO formation. F) Series-parallel reaction network of CH_3OH synthesis with rate constants measured from kinetic analysis.

S7. Thermodynamic and transport effects on tandem conversion

S7.1. When CH_3OH synthesis from CO_2 reaches thermodynamic equilibrium

To reach thermodynamic equilibrium for CH_3OH synthesis under tandem reaction conditions, we increased the amount of $ZnZrO_x$ to 1g in interpellet and intrapellet admixtures to increase the partial pressure of CH_3OH, thereby to increase the reaction quotient ($Q = \frac{P_{CH_3OH,eff} P_{H_2O} P^{\circ 2}_{STD}}{P_{CO_2} P^3_{H_2}}$) and approach to equilibrium ($z = \frac{Q}{K_p}$) values.

During CO_2 hydrogenation at 350 °C and 500 psig over interpellet and intrapellet mixtures with $ZnZrO_x$:MFI ratio 2:1, *z* was found to be 1.02 and 1.05, respectively, indicating CH_3OH synthesis reaction reached thermodynamic equilibrium. Therefore, the rate enhancement $\frac{STY_{intrapellet,obs}}{STY_{interpellet,obs}}$=1.095 in **Fig. S3B** could be attributed to a forward shift in CH_3OH synthesis equilibrium.

Similarly, equilibrium was achieved for interpellet and intrapellet mixtures with $ZnZrO_x$:MFI ratio 1:2, however, more paraffins were observed due to secondary hydrogenation of olefins with an increased amount of acid sites (**Fig. S3C**). Approach to equilibrium *z* was found to be 1.13 and 1.24 over interepellet and intrapellet cases, respectively. The rate enhancement $\frac{STY_{intrapellet,obs}}{STY_{interpellet,obs}}$=1.14 (**Fig. S3D**) was slightly more higher in this case likely due to the presence of more acid sites and a higher consumption rate of CH_3OH.

It is to be noted that while theoretically *z* has to be ≤1, for these tandem reaction cases, *z* can be greater than 1 as $P_{CH_3OH,eff}\,(P_{CH_3OH} + P_{HC})$ is calculated assuming all hydrocarbon products originates from CH_3OH. Therefore, $z \geq 1$ likely indicates a forward shift in thermodynamic equilibrium due to the consumption of intermediate CH_3OH over acid sites.

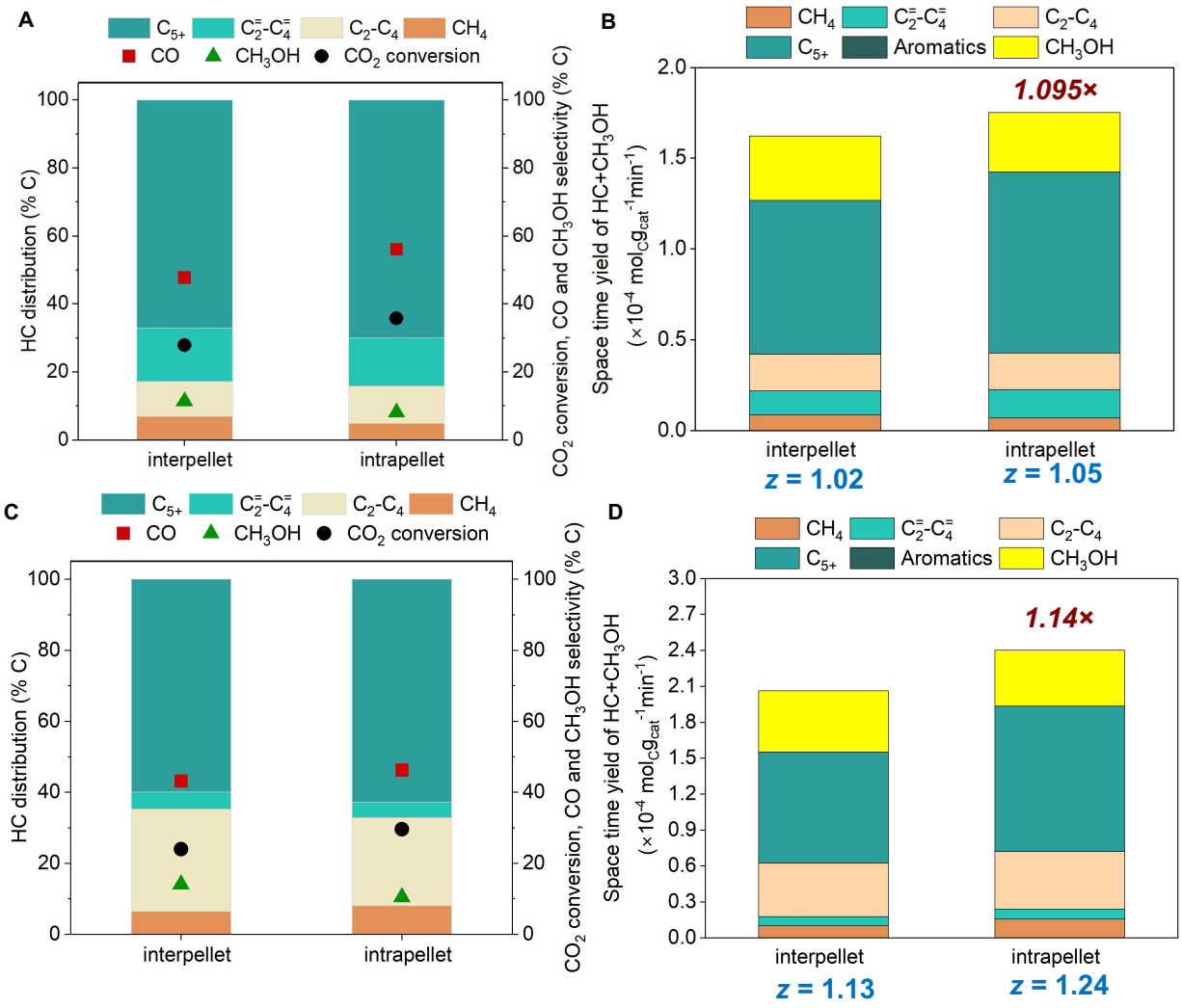

Fig. S3: Tandem CO_2 hydrogenation over interpellet and intrapellet mixtures of $ZnZrO_x$ and MFI (Si:Al ratio 40, CBV 8014 from zeolyst). A) Hydrocarbon distribution, CO_2 conversion, CO and CH_3OH selectivity; B) STY of HC and CH_3OH over interpellet and intrapellet mixtures with $ZnZrO_x$:MFI ratio 2:1. Reaction conditions: 350 °C, 500 psig, total flow 150 ml/min, $ZnZrO_x$ 1g, HZSM-5 0.5 g, total catalyst 1.5 g. C) Hydrocarbon distribution, CO_2 conversion, CO and CH_3OH selectivity; D) STY of HC and CH_3OH over interpellet and intrapellet mixtures with $ZnZrO_x$:MFI ratio 1:2. Reaction conditions, 350 °C, 500 psig, 280 ml/min, $ZnZrO_x$ 1g, HZSM-5 2 g, total catalyst 3 g.

S7.2. When CH_3OH synthesis does not approach to equilibrium

We conducted CO_2 hydrogenation over different metal oxides ($ZnZrO_x$ and Cr_2O_3) and zeolite/zeotype (MFI and SAPO-34) combinations away from equilibrium ($z < 0.5$, see **Fig. S4B**).

Fig. S4C depicts the catalytic performance of interpellet and intrapellet mixtures for $ZnZrO_x$/SAPO-34, Cr_2O_3 /SAPO-34, and $ZnZrO_x$/MFI systems. Across all three systems, intrapellet mixtures exhibited higher STY of combined HC and CH_3OH+DME (~1.1-1.4×), as compared to interpellet mixtures, which cannot be solely explained by equilibrium shift. The predicted rate enhancement from the transport resistance model ($\frac{r_{intrapellet,obs}}{r_{interpellet,obs}} = \frac{\eta_4 r_{intrinsic}}{\eta_1 \eta_3 \eta_4 r_{intrinsic}} = \frac{1}{\eta_1 \eta_3}$ ~1.22-1.43) was found to be similar to observed rates.

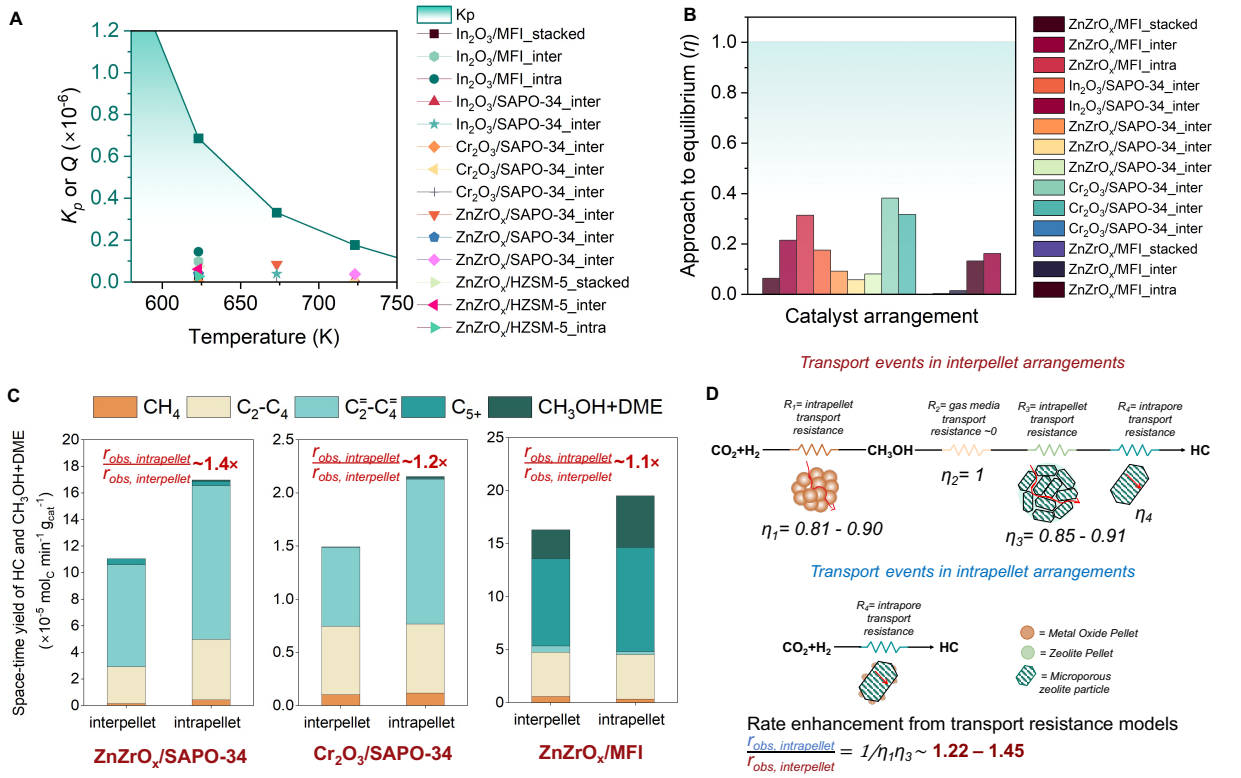

Fig. S4: A) Comparison of calculated reaction quotient Q from reactant and product partial pressures during CO_2 hydrogenation over different metal oxide and zeolite combinations, and calculated equilibrium constant K from Gibbs free energy at different reaction temperatures. B) Calculated approach to equilibrium during tandem CO_2 hydrogenation indicated CH_3OH synthesis reaction was away from equilibrium (z<1). C) Comparison of combined space-time yield of CH_3OH and HC over different metal oxide and zeolite systems. Reaction conditions, 350 °C, 3 MPa, 150-280 sccm total flow, H_2:CO_2 ratio 3:1, metal oxide : zeolite mass ratio 1:1, 1g catalyst. D) Proposed reaction-transport resistance model for interpellet and intrapellet oxide/zeolite mixtures.

S8. Effectiveness factor calculations

S8.1. Effectiveness factor for intrapellet transport resistances

Effectiveness factor for intrapellet transport resistance was calculated by independent size-dependent studies.
Assuming a first-order reaction in a spherical catalyst pellet,

$$\eta = \frac{3}{\phi_1^2}(\phi_1 coth\phi_1 - 1) \quad \text{(S12)}$$

Weisz–Prater parameter:

$$C_{wp} = \eta\phi_1^2 = \frac{-r_A(obs)\rho_c R^2}{D_e C_{As}} \quad \text{(S13)}$$

Sample calculation is shown in **Table S5** for methanol synthesis.

Table S5: Conversion of CO_2 to CH_3OH with different pellet sizes of $ZnZrO_x$. Reaction conditions: 350 ℃, 500 psig, total flow 280 mL/min, H_2:CO_2 ratio 3:1.

Run	Reaction rate, r_A ($mol_C min^{-1} g_{cat}^{-1}$)	Pellet size (micron)
1	7.17×10^{-4}	422.5
2	7.72×10^{-4}	213.5
3	7.94×10^{-4}	108.5

Combining Eq. S12 and S13,

$$\frac{-r_A(obs)\rho_c R^2}{D_e C_{As}} = \eta\phi_1^2 = 3(\phi_1 coth\phi_1 - 1) \quad \text{(S14)}$$

Applying (Eq-S14) to Runs 1 and 2, and taking the ratio, then the terms ρ_c, D_e, and C_{As} cancel because the runs were carried out under identical conditions. Therefore, the ratio becomes,

$$\frac{-r_{A2}R_2^2}{-r_{A1}R_1^2} = \frac{\phi_{12}coth\phi_{12} - 1}{\phi_{11}coth\phi_{11} - 1}$$

Thiele modulus,

$$\phi_1 = R\sqrt{\frac{-r_{As}\rho_c}{D_e C_{As}}}$$

Taking the ratio of the Thiele moduli for runs 1 and 2

$$\frac{\phi_{11}}{\phi_{12}} = \frac{R_1}{R_2}$$

Solving these equations for runs 1 and 2,

$$\phi_{11} = 1.278$$
$$\phi_{12} = 0.645$$

Similarly, ϕ_{13} was found to be 0.389.

Correspondingly the effectiveness factor would be,

$$\eta_{11} = \frac{3}{\phi_{11}^2}(\phi_{11} coth\phi_{11} - 1) = 0.906$$
$$\eta_{12} = \frac{3}{\phi_{12}^2}(\phi_{12} coth\phi_{12} - 1) = 0.973$$

Similarly, η_{13} was found to be 0.99 for 120-170 mesh size (108.5 μm) particles.

We applied the same method for calculating the effectiveness factor associated with clusters of $ZnZrO_x$ in intrapellet mixtures. In this case, we conducted CH_3OH synthesis reaction over intrapellet mixtures of $ZnZrO_x$ and silicalte-1 (S-1) under same reaction conditions. The cluster size was estimated to be ~30 nm based on TEM image (**Fig. S5**). The reaction rate was found to be 7.92×10^{-4} $mol_C min^{-1} g_{cat}^{-1}$, indicating effectiveness factor η_1 ~1.

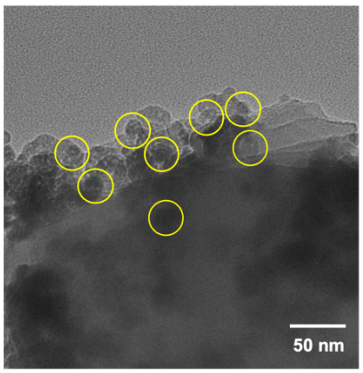

Fig. S5: Transmission electron micrograph (TEM) of intrapellet mixture of $ZnZrO_x$/S-1.

S8.2. Estimation of overall effectiveness factor for a series of transport resistances

For a steady-state, isothermal system, assuming first order rate expression, r = kC

For sequential diffusion: *e.g.,* macropore → micropore

For micropore domain:
Intrinsic rate: $r_{micro,intrinsic} = k \cdot C_m$
Actual rate: $r_{micro,actual} = \eta_{micro} \cdot k \cdot C_m$

For macropore domain:
$r_{macro,actual} = \eta_{macro} \cdot (\eta_{micro} \cdot k \cdot C_m)$

Therefore, overall effectiveness can be estimated as: [33]
$\eta_{total} = (r_{macro,actual}) / (k \cdot C_m) = \eta_{macro} \cdot \eta_{micro}$

S9. Acidity characterization of zeolites

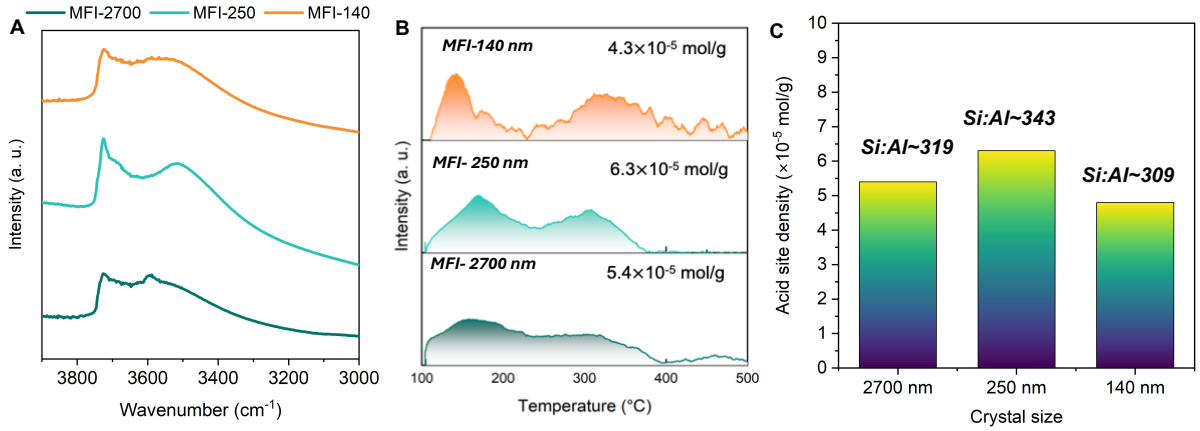

Fig. S6: A) Transmission FTIR spectroscopy for MFI-140, MFI-250 and MFI-2700. The bands around 3580-3650 cm^{-1} range are associated with bridging hydroxyls (BAS) and the bands, while the bands around 3720-3730 cm^{-1} are associated with silanol groups. B) Acid sites quantified by NH_3-temperature programmed desorption (TPD). C) Comparison of the number of acid sites from NH_3-TPD and Si/Al ratio from EDS for three different crystal sizes.

S10. Structural, textural, and morphological properties of zeolites

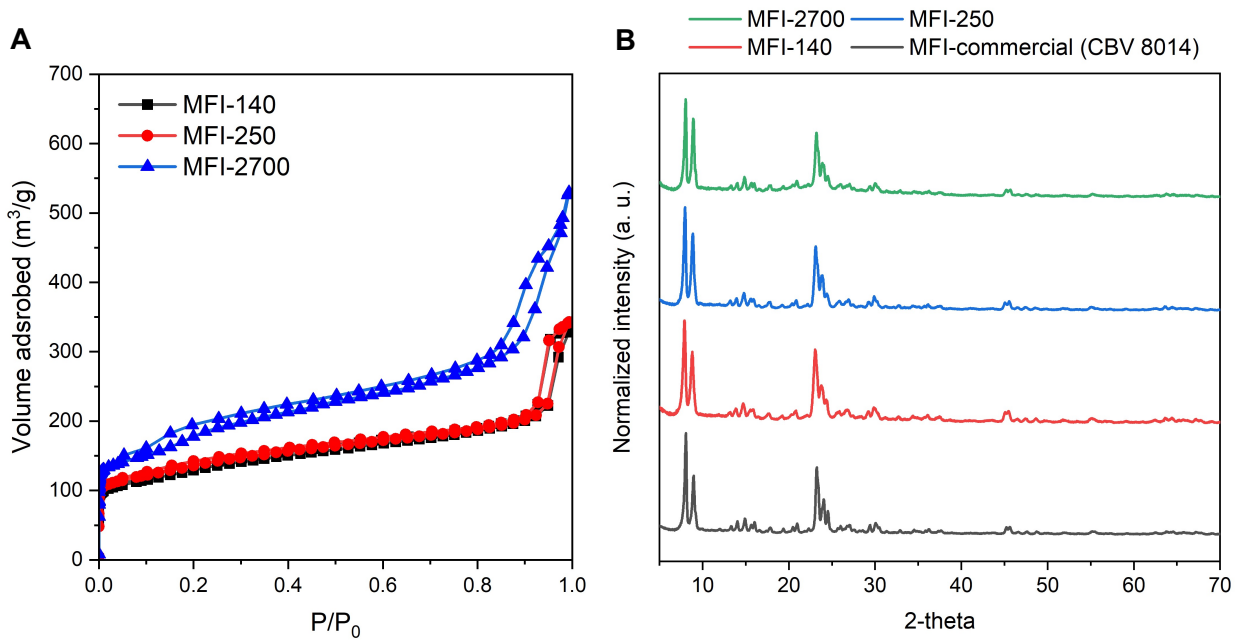

Fig. S7: A) Nitrogen physisorption isotherm and B) PXRD for MFI with different crystal sizes.

Table S6: Physisorption analysis of MFI samples and $ZnZrO_x$.

		BET surface area	Slope	BET int	Corr. Coeff. BET	Pore vol	t-plot	Micro pore vol	Micro pore area	External surface area	Corr. Coeff.
Sample	P/Po	m^2/g	1/g	1/g		cc/g	P/Po	cc/g	m^2/g	m^2/g	
MFI-140	0.00002-0.05	447.83	7.77	3.1E-03	1.00	0.51	0.2-0.5	0.11	232.7	215.12	0.999
MFI-250	0.00002-0.05	474.19	7.34	2.7E-03	0.99	0.53	0.2-0.5	0.12	265.7	208.50	0.999
MFI-2700	0.00002-0.05	582.02	5.98	2.3E-03	1.00	0.81	0.2-0.5	0.13	225.4	356.60	0.994
$ZnZrO_x$	0.05-0.3	68.7	49.74	9.08E-01	0.99	0.11	-	-	-	-	-

S11. Structural, textural and morphological properties of $ZnZrO_x$

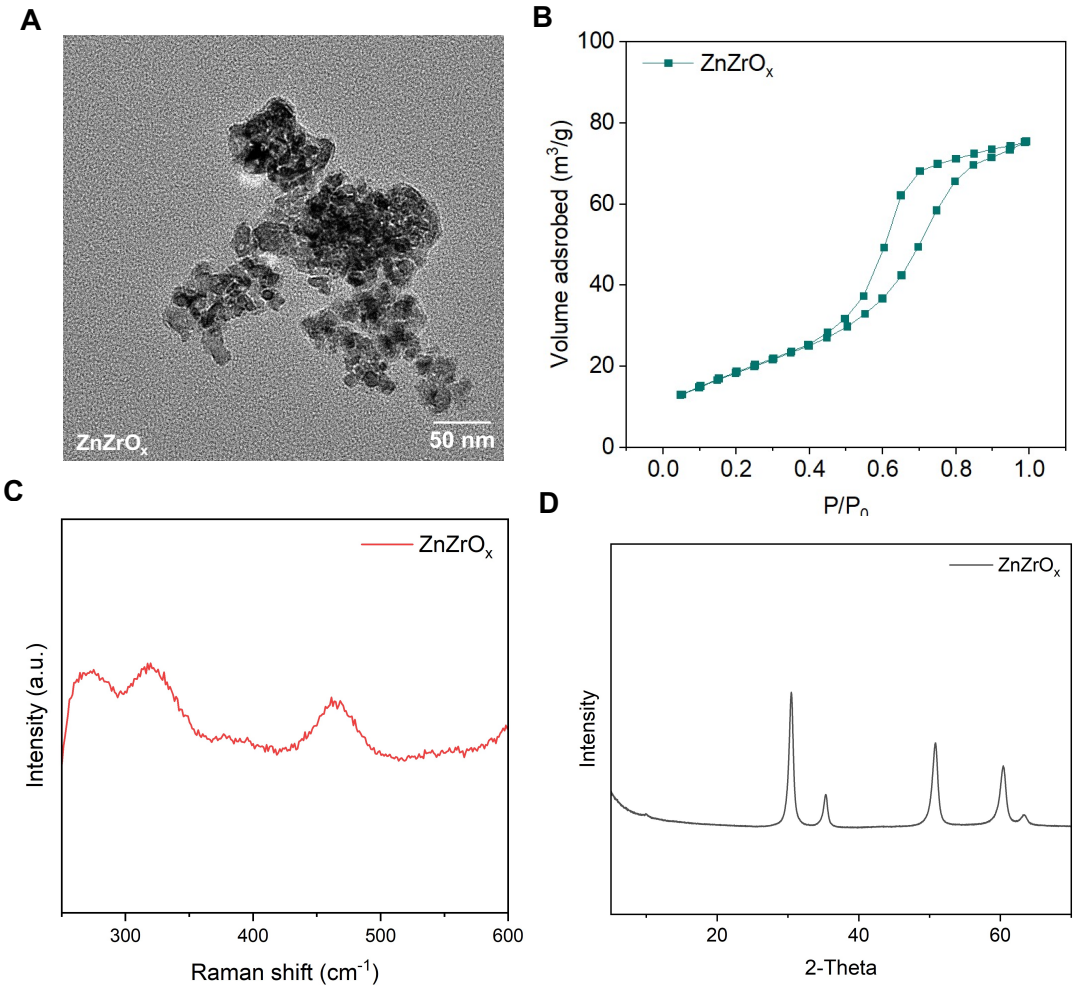

Fig. S8: A) Transmission electron micrograph of $ZnZrO_x$ showing an average particle size of ~10 nm. B) N_2 physisorption isotherm for $ZnZrO_x$, exhibiting mesoporous type IV isotherm.[34] C) Raman spectroscopy of $ZnZrO_x$ exhibited bands at 265, 320, and 460 cm^{-1}, which is attributed to the tetragonal phase.[35] D) PXRD pattern $ZnZrO_x$, showing tetragonal phase of $ZnZrO_x$ at 30.5° (011), 35.4° (110), 50.9° (112), and 60.5° (121).[20]

S12. Stability test during CO_2 hydrogenation

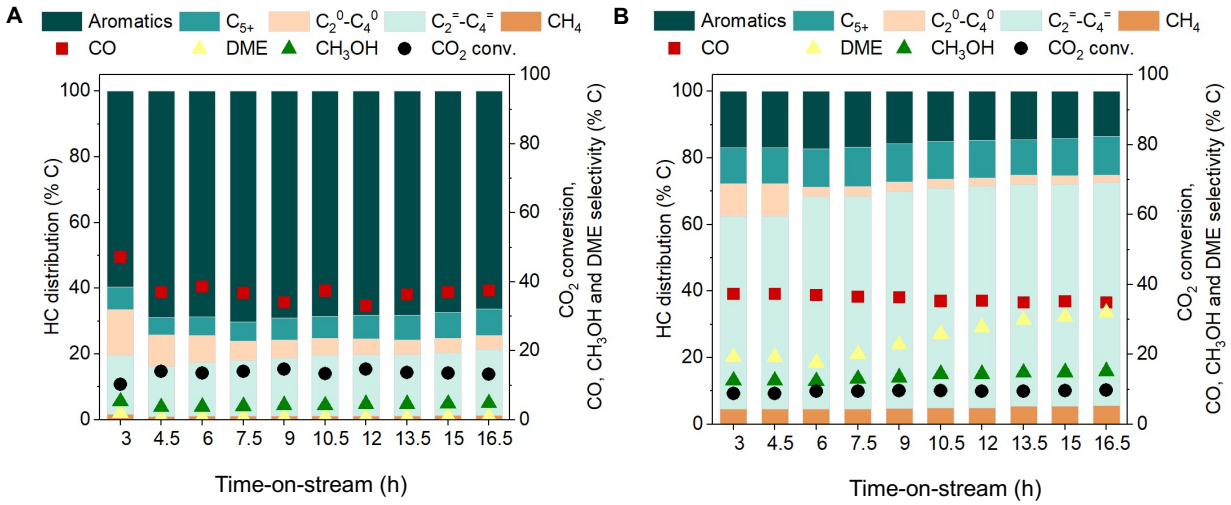

Fig. S9: Time-on-stream (TOS) data during CO_2 hydrogenation over intrapellet mixture of ZnZrOx and A) MFI-140 and B) MFI-2700. Reaction conditions: 350 °C, 500 psig, H_2:CO_2 ratio 3:1, total flow 280 ml/min, $ZnZrO_x$ 0.3 g, MFI 0.3 g, total catalyst 0.6 g. The catalyst was pretreated in 5% H_2 (balance N_2) at 300°C for 1 h and cooled to 40 °C prior to the reaction. Left axis shows HC distribution and right axis shows CO_2 conversion, CO and CH_3OH+DME selectivity. While no deactivation was observed for MFI-140, MFI-2700 deactivated after 9h, thereby reducing C-C coupling and increasing CH_3OH and DME selectivity.

S13. Analysis of hydrocarbon pool (HP) propagation during CO_2 hydrogenation over different crystal sizes of MFI

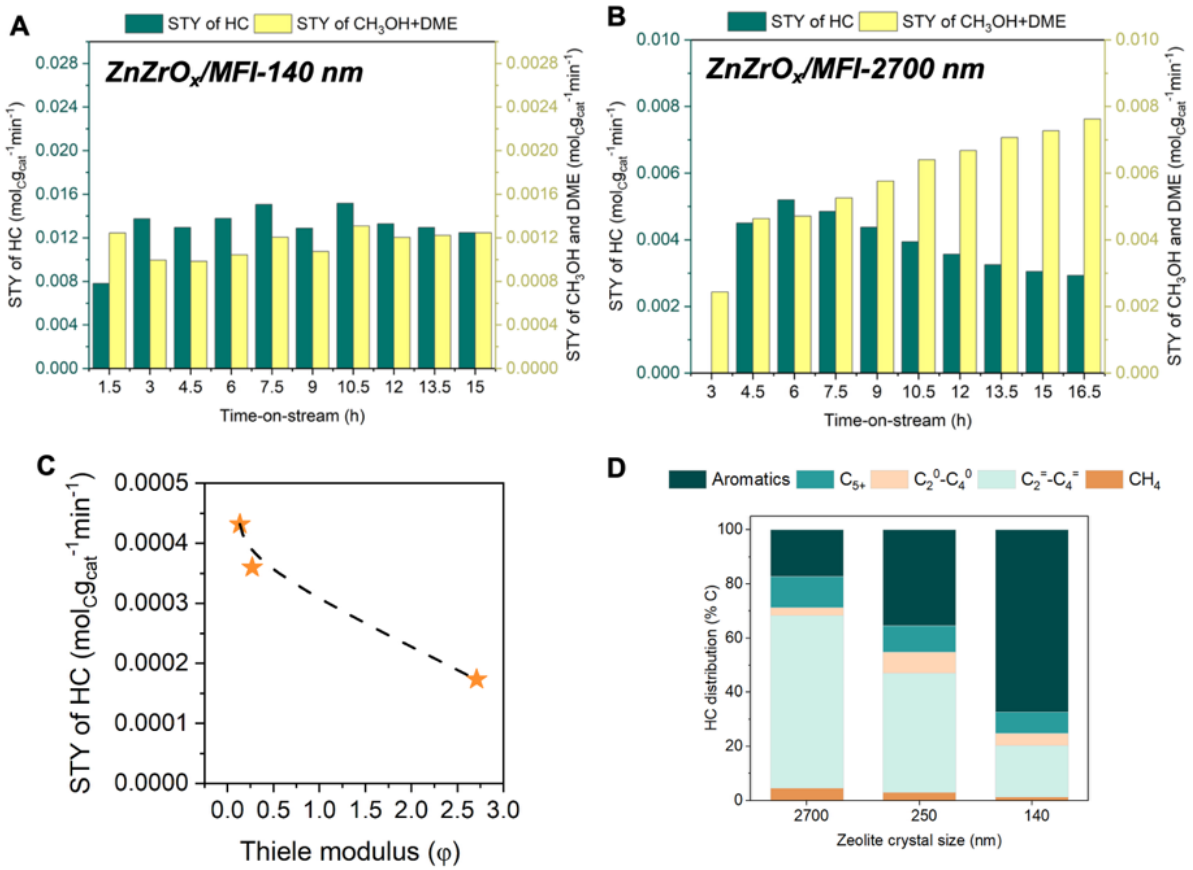

Fig. S10: Space-time yield (STY) of HC and oxygenates during CO_2 hydrogenation over intrapellet mixture of $ZnZrO_x$ and A) MFI-140 and B) MFI-2700. Reaction conditions: 350 °C, 500 psig, H_2:CO_2 ratio 3:1, total flow 280 ml/min, $ZnZrO_x$ 0.3 g, MFI 0.3 g, total catalyst 0.6 g. While no deactivation was observed for MFI-140, MFI-2700 deactivated after 9h, thereby decreasing HC STY while CH_3OH and DME STY increased. C) Space-time yield (STY) of HC with respect to the calculated Thiele modulus. D) HC distribution during CO_2 hydrogenation over intrapellet mixture of $ZnZrO_x$ with MFI-140, MFI-250 and MFI-2700

We arranged the as-synthesized MFI samples with $ZnZrO_x$ as intrapellet mixtures to isolate the influence of R_4. During time-on-stream studies, under identical reaction conditions, MFI-140 did not show any deactivation over 15 h of reaction; however, MFI-2700 progressively deactivated as STY of HC dropped while STY of CH_3OH and DME increased. These trends indicate a loss in C-C coupling ability in MFI-2700, likely *via* coking.

We interrogated the HCP reaction network to identify the reaction pathways that cause deactivation under intracrystalline diffusion constraints. The total STY of HC can be expressed with a triple summation as,

$$Total\ STY of\ HC = \frac{1}{g_{cat}} \sum_{m} \sum_{n} \sum_{p} m v_{C_m H_n, p} r_p^{obs} \tag{S15}$$

Where $\nu_{,C_mH_n}$ represents the stoichiometric coefficient associated with C_mH_n in the reaction p, and r_p^{obs} is the observed volumetric rate of reaction p under diffusion limitation.

If STY decreased with increasing zeolite crystal size or Thiele modulus, as observed in **Fig. S10C**, it would satisfy the following inequality,

$$\frac{\partial}{\partial \varphi}\left[\sum_{m}\sum_{n}\sum_{p} m v_{C_mH_n,p} r_p^{obs}\right] < 0 \qquad \text{(S16)}$$

The reactions within the complex reaction network for MTH conversion with non-zero $\nu_{C_mH_n}$ comprise methylation, oligomerization, β-scission, dealkylation, hydrogen transfer, and aromatization. Rates of oligomerization, β-scission, and hydrogen transfer cancel, ultimately, in the m-weighted sum over all effluent hydrocarbon products (sums with indices m and n) and $\nu_{,C_mH_n}$ weighted sum over all reactions (sum with index p). For example, the oligomerization of C_aH_c with C_bH_d,

$C_aH_c + C_bH_d \overset{p*}{\rightarrow} C_{a+b}H_{c+d}$

The observed rate of consumption of C_aH_c and C_bH_d *via* oligomerization is canceled exactly by the rate of formation of oligomer $C_{a+b}H_{c+d}$ *via* the identical reaction, i.e., $\sum_m \sum_n m v_{C_mH_n,p} r_{p*}^{obs}$= [*a* (-1) + *b* (-1)+ (*a*+*b*) (1)] $r_{p*}^{obs} = 0$

Similarly, the rates of consumption of reactants and rates of formation of products in β -scission reactions cancel exactly in the reverse oligomerization reaction. The rate of consumption of C_aH_c and C_bH_d by hydrogen transfer is canceled by the formation of $C_aH_{c\pm2}$ and $C_bH_{d\pm2}$. Therefore, only olefin methylation, aromatization, and aromatics dealkylation contribute, ultimately, to the inequality in Eq. S16.

Despite TOS studies and 2-MB/C_2 ratio (**Fig. 5E**) indicating aromatic pool is more favored over MFI-2700, the HC distribution showed an opposite trend (see **Fig. S10D**) where MFI-2700 showed the least aromatic selectivity (17%) as compared to MFI-140 and MFI-250 (67% and 35%, respectively). To further understand this anomaly, we tracked the selectivity of ethylene (C_2), propylene (C_3) and 2-MB (**Fig. 5F**). While C_2 and C_3 can originate from the aromatic pool *via* dealkylation as terminal products, 2-MB comes exclusively from the olefin pool. We observed that C_2 and C_3 selectivity increased (from 11.94% to 23.61% and from 9.8% to 36.4%, respectively, as crystal size increased from 140 to 2700 nm), while 2-MB dropped (3.8% to 1.8%). These opposite trends further corroborated that with increasing the acid site domain and diffusion limitation, aromatic pool was favored, which in turn enhanced the formation of C_2 and C_3 *via* dealkylation. This is further indicated by the aromatic product distribution (**Fig. 5G**), where increasing crystal size shifted the aromatic distribution to less methylated products, indicating towards aromatic dealkylation under enhanced diffusion limitations.

Integrating our experimental findings and theoretical assessments on the MTH network, we infer that under strong diffusion limitation, CH_3OH undergoes C-C coupling to form olefins, olefins undergo aromatization, and then aromatics undergo dealkylation to form C_2 and C_3. Therefore, the HCP mechanism can be simplified as a consecutive series reaction network (CH_3OH→olefins→aromatics→C_2,C_3).

S14. Reaction diffusion formalisms

Here, we derive expressions describing measured hydrocarbon product selectivities formed over acid sites during CO_2 hydrogenation. Reactions are all assumed to be pseudo-first order. Reverse reactions are neglected. Acid domains are assumed to be spherical with a size R. Assuming sufficient intimacy of physical mixtures, which is a reasonable assumption for intrapellet mixtures.

Product selectivities are assessed for B, C, and D, as defined in A→B→C→D ; A is CH_3OH, B is the lump of C_{4+} olefins, C is the lump of aromatics, and D dealkylation products ethylene+propylene. Species A, B, C, and D have diffusivities $D_A, D_B, D_C,$ and D_D, respectively, where $D_A > D_D > D_B > D_C$. We assume that A is not diffusion-limited, as the kinetic diameter of CH_3OH is much smaller than the MFI cage size. Steady-state mass balances on B, C, and D can be expressed as:

$$D_B \frac{1}{r^2}\frac{d}{dr}\left(r^2 \frac{dC_B}{dr}\right) = k_B \rho_H^+ C_B - k_A \rho_H^+ C_{A,0} \quad \text{(S17)}$$

$$D_C \frac{1}{r^2}\frac{d}{dr}\left(r^2 \frac{dC_C}{dr}\right) = k_C \rho_H^+ C_C - k_B \rho_H^+ C_B \quad \text{(S18)}$$

$$D_D \frac{1}{r^2}\frac{d}{dr}\left(r^2 \frac{dC_D}{dr}\right) = -k_C \rho_H^+ C_C \quad \text{(S19)}$$

C_x is the concentration of species x, $C_{A,0}$ is the equilibrium pressure of CH_3OH set by the redox sites on zeolite surface, r is radius, and ρ_H^+ is proton density.

Solving these ordinary differential equations with boundary conditions:

$$\frac{dC_B}{dr}|_{r=0} = \frac{dC_C}{dr}|_{r=0} \frac{dC_D}{dr}|_{r=0} = 0$$

$$C_{B,0} = C_{C,0} = C_{D,0} = 0$$

Defining dimensionless variables:

Length:

$$\zeta = \frac{r}{R} \quad \text{(S20)}$$

Concentration:

$$Y_A = C_A / C_{A,0} \quad \text{(S21)}$$

$$Y_B = \frac{k_B C_B}{k_A C_{A,0}} \quad \text{(S22)}$$

$$Y_C = \frac{k_C C_C}{k_A C_{A,0}} \quad \text{(S23)}$$

$$Y_D = C_D / C_{A,0} \quad \text{(S24)}$$

Defining dimensionless parameters:

Thiele moduli:

$$\phi_A^2 = \frac{k_A \rho_H^+ R^2}{D_A} \tag{S24}$$

$$\phi_B^2 = \frac{k_B \rho_H^+ R^2}{D_B} \tag{S26}$$

$$\phi_C^2 = \frac{k_C \rho_H^+ R^2}{D_C} \tag{S27}$$

$$\Theta_{CB} = \frac{\phi_C^2}{\phi_C^2 - \phi_B^2} \tag{S28}$$

$$\psi^2 = \frac{D_A}{D_D} \tag{S29}$$

Non-dimensionalizing Equations S17-19 and the boundary conditions yields:

$$\frac{1}{\zeta^2}\frac{d}{d\zeta}\left(\zeta^2 \frac{dY_B}{d\zeta}\right) = \phi_B^2 (Y_B - 1) \tag{S30}$$

$$\frac{1}{\zeta^2}\frac{d}{d\zeta}\left(\zeta^2 \frac{dY_C}{d\zeta}\right) = \phi_C^2 (Y_C - Y_B) \tag{S31}$$

$$\frac{1}{\zeta^2}\frac{d}{d\zeta}\left(\zeta^2 \frac{dY_D}{d\zeta}\right) = -\phi_A^2 \psi^2 Y_C \tag{S32}$$

$$\frac{dY_B}{d\zeta}|_{\zeta=0} = 0 \tag{S33}$$

$$Y_B|_{\zeta=1} = 0 \tag{S34}$$

$$\frac{dY_C}{d\zeta}|_{\zeta=0} = 0 \tag{S35}$$

$$Y_C|_{\zeta=1} = 0 \tag{S36}$$

$$\frac{dY_D}{d\zeta}|_{\zeta=0} = 0 \tag{S37}$$

$$Y_D|_{\zeta=1} = 0 \tag{S38}$$

Solving equations S30-32, we obtain analytical expressions for concentration profiles:

$$Y_B(\zeta) = 1 - \frac{1}{\zeta}\frac{\sinh(\phi_B\zeta)}{\sinh(\phi_B)} \tag{S39}$$

$$Y_C(\zeta) = 1 - \frac{1}{\zeta}\left((1-\Theta_{CB})\frac{\sinh(\phi_C\zeta)}{\sinh(\phi_C)} + \Theta_{CB}\frac{\sinh(\phi_B\zeta)}{\sinh(\phi_B)}\right) \tag{S40}$$

$$Y_D(\zeta) = \frac{\phi_A^2\psi^2}{\zeta}\left(\frac{1}{\phi_C^2}\frac{\sinh(\phi_C\zeta)}{\sinh(\phi_C)} + \Theta_{CB}\left(\frac{1}{\phi_B^2}\frac{\sinh(\phi_B\zeta)}{\sinh(\phi_B)} - \frac{1}{\phi_C^2}\frac{\sinh(\phi_C\zeta)}{\sinh(\phi_C)}\right)\right) - \phi_A^2\psi^2\frac{\zeta^2-1}{6} - \phi_A^2\psi^2\left(\frac{1}{\phi^2} + \Theta_{CB}\left(\frac{1}{\phi_B^2} - \frac{1}{\phi_C^2}\right)\right) \tag{S41}$$

Equations S39-41 describe concentration profiles for each species. Concentration profiles can be expressed in terms of selectivities. At steady state, the diffusion rate of a species is equivalent to its measured rate of formation. Thus, expressions for selectivity are derived by taking the diffusion rate for each species, with respect to the volumetric rate of reactant consumption.

Selectivity to B:

$$S_B = \frac{3}{\phi_B^2}(\phi_B\coth(\phi_B) - 1) \tag{S42}$$

Selectivity to C:

$$S_C = \frac{3}{\phi_C^2}\left(1 - \frac{\phi_C^2}{\phi_C^2 - \phi_B^2}\right)\phi_C\coth(\phi_C) + \frac{\phi_C^2}{\phi_C^2 - \phi_B^2}\phi_B\coth(\phi_B) - 1) \tag{S43}$$

Selectivity to D:

$$S_D = 1 + 3\left(\frac{1}{\phi_C^2} - \frac{\coth(\phi_C)}{\phi_C} - \frac{\phi_C^2}{\phi_C^2 - \phi_B^2}\left(\frac{\coth(\phi_B)}{\phi_B} - \frac{\coth(\phi_C)}{\phi_C} + \frac{1}{\phi_C^2} - \frac{1}{\phi_B^2}\right)\right) \tag{S44}$$

By using $\frac{\phi_B}{\phi_A} = 20.36$ and $\frac{\phi_C}{\phi_A} = 2.56$ from experimentally measured values, S_B, S_C and S_D were plotted for a range of ϕ_A. The theoretical trend of selectivity with respect to ϕ_A was compared with experimentally observed selectivities for different acid domain sizes of zeolites.

S15. DRIFTS during methanol temperature programmed surface reaction (TPSR)

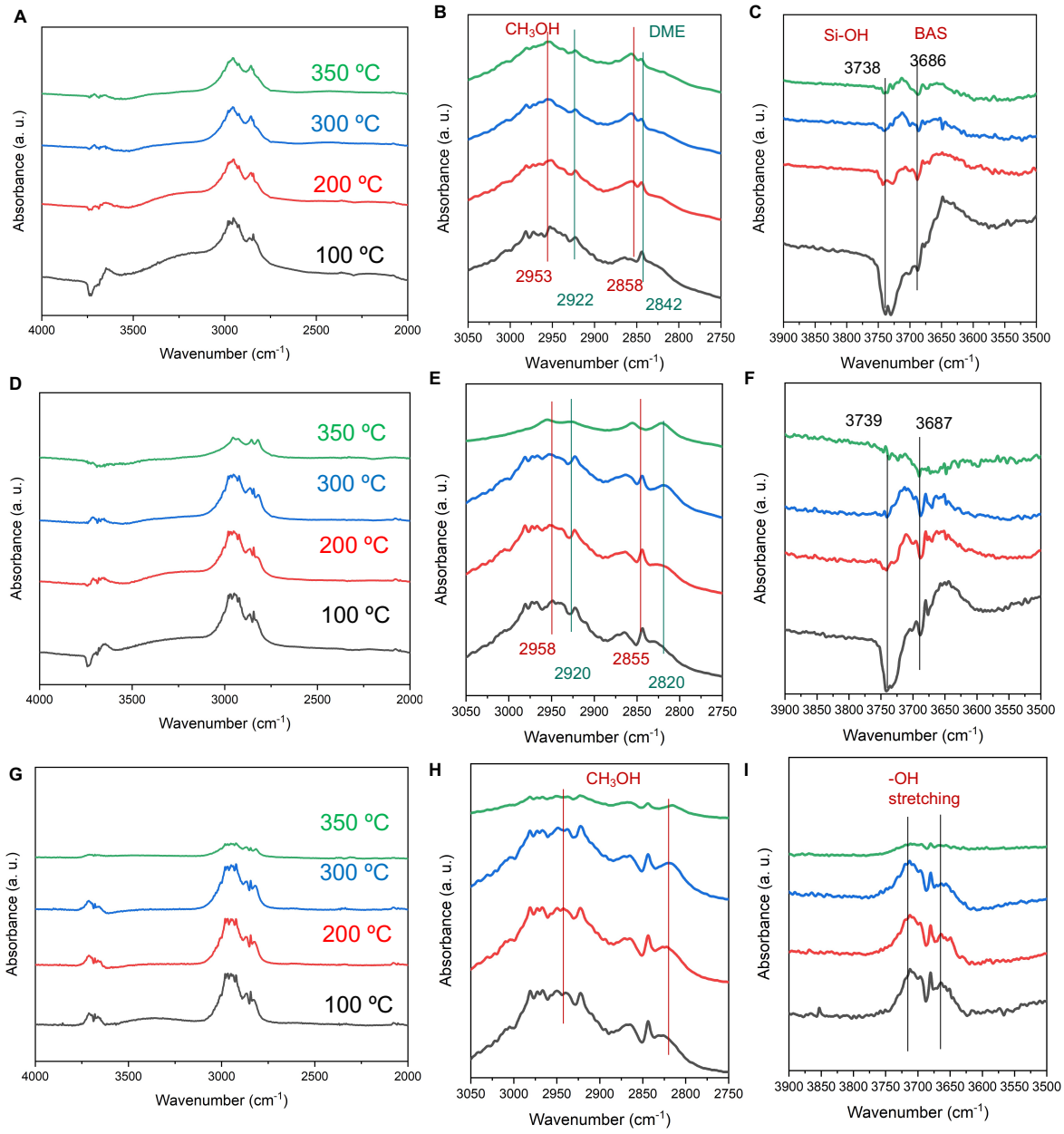

Fig. S11: DRIFTS during CH_3OH TPSR over A-C) MFI-140, D-F) intrapellet $ZnZrO_x$/MFI-140 and G-I) $ZnZrO_x$ form wavenumber 4000-2000 cm^{-1}. The spectra were collected using sample spectra under N_2 at the specific temperatures as background to observe the surface intermediates without zeolite or $ZnZrO_x$ overtones.

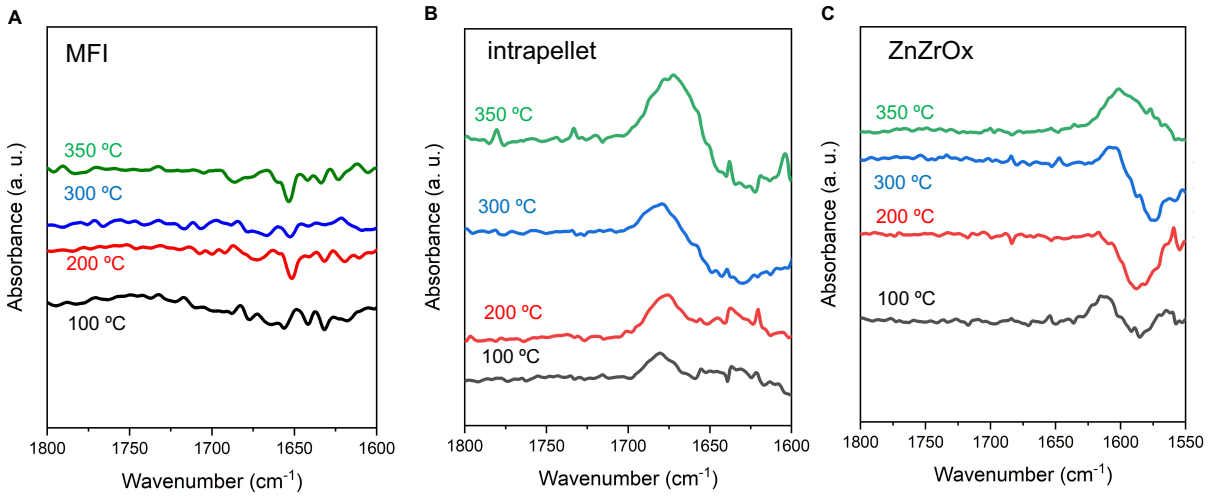

Fig. S12: DRIFTS during CH_3OH TPSR over A) MFI-140, B) intrapellet $ZnZrO_x$/MFI-140, and C) $ZnZrO_x$ form wavenumber 1600-1800 cm^{-1}. The spectra were collected using sample spectra under N_2 at the specific temperatures as background to observe the surface intermediates without zeolite or $ZnZrO_x$ overtones.

S16. Sample calculation of carbon balance

Table S7: Sample calculation of carbon balance during CO_2 hydrogenation reaction over interpellet and intrapellet $ZnZrO_x$ and MFI-140 mixtures. Reaction conditions: 350 °C,500 psig, total flow 280 mL/min, H_2:CO_2 ratio 3:1, $ZnZrO_x$:MFI mass ratio 1:1, total catalyst 0.6 g.

Catalyst	T (°C)	CO_2 in (%C)	C_{in} ($C_{CO_2,\ inlet} \times F_{inlet}$) ($\times 10^{-3}$ mol_C/min)	CO_2 out (%C)	$C_{CO_2,\ outlet} \times F_{outlet}$ ($\times 10^{-3}$ mol_C/min)	CO_2 conv.	sum of C in HC (%C)	sum of C in CO (%C)	sum of C in CH_3OH + DME (%C)	C_{out} (product+ unconverted CO_2) ($\times 10^{-3}$ mol_C/min)	CO_2 conv. internal norm. (%C)	C balance (%)
interpellet _$ZnZrO_x$/ MFI-140	350	25	**3.12**	23.45	2.91	6.9	1.10	0.47	0.22	**3.23**	7.07	**103.52**
intrapellet _$ZnZrO_x$/ MFI-140	350	25	**3.12**	22.30	2.76	11.4	1.09	0.83	0.43	**2.97**	9.55	**95.20**

$$CO_2 \text{ conversion, } X_{CO_2} = \frac{C_{CO_2,\ inlet} \cdot F_{inlet} - C_{CO_2,\ outlet} \cdot F_{outlet}}{C_{CO_2,\ inlet} \cdot F_{inlet}} \times 100\% \quad \text{(S45)}$$

Internal normalization method,

$$CO_2 \text{conversion, } X_{CO_2,\text{internal normalization}} = \frac{RRF_{CH_3OH} \times A_{CH_3OH} + RRF_{CO} \times A_{CO} + \sum_1^n RRF_{C_nH_m} \times A_{C_nH_m}}{RRF_{CO_{2,outlet}} \times A_{CO_{2,outlet}} + RRF_{CH_3OH} \times A_{CH_3OH} + RRF_{CO} \times A_{CO} + \sum_1^n RRF_{C_nH_m} \times A_{C_nH_m}} \times 100\% \quad \text{(S46)}$$

$$\text{C balance} = \frac{C_{in} - C_{out}}{C_{in}} \times 100\% \quad \text{(S47)}$$

Where $C_{CO_2,\ inlet}$ and $C_{CO_2,\ outlet}$ are the concentrations of CO_2 at the inlet and outlet, respectively. F_{inlet} and F_{outlet} are the inlet and outlet gas flow rates of the reactor. RRF is the relative response factor, and A is the peak area of the species on chromatographic spectra.

S17. Process analysis of tandem CO_2 hydrogenation

Process simulation was performed in Aspen HYSYS v12. For the design of a rigorous distillation column, we first apply Shortcut distillation models to estimate the design parameters (e.g., tray number, reflux ratio, condenser/reboiler duties). These parameters are then supplied as initial guesses for the rigorous distillation columns. Cryogenic distillation was needed for the separation of the CO. For flash drums and three-phase separators, target operating conditions such as temperature and pressure are specified as necessary for the required separations. Other units, such as heaters and compressors, are systematically introduced to adjust the process streams to those conditions. The heat exchangers and compressors are considered essential process units necessary to achieve the desired separation. The capital and utility costs of PSA membranes[36-38] and molecular sieves[39] are obtained from published correlations, while their separation behavior is represented in Aspen HYSYS using generic separator models that capture the material balances. Energy integration is conducted within the Aspen Energy Analyzer through a methodical two-phase approach: (i) an initial targeting analysis aimed at ascertaining the maximum potential for heat recovery, and (ii) the automated synthesis of the Heat Exchanger Network (HEN) to actualize those energy savings. Consequently, each process block is not solely balanced in terms of mass and energy but is also thermally optimized within the confines of the simulation environment. All primary feedstocks enter the process at 1 bar and 30^{o} C in the base case. Purchase equipment cost and utility consumption are obtained from Aspen Process Economic Analyzer. Reactors are modeled as stoichiometric units, with catalyst costs calculated using the step method and reactor vessels priced as jacketed vessels.[40] Syngas-to-methanol reactor data was taken from Park et al. (2014).[42] It was assumed that 100% of methanol is converted to hydrocarbons.

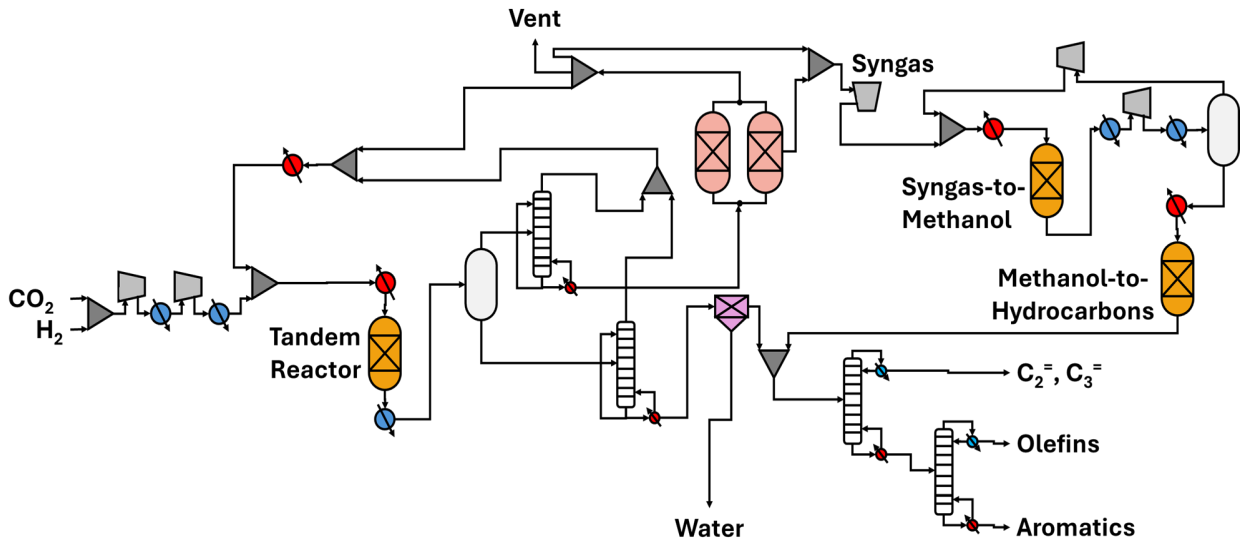

Fig. S13: Process simulation.

Table S8: Process simulation parameters.

Name	Vapor Fraction	Temperature [C]	Pressure [kPa]	Molar Flow [kgmole/h]	Mass Flow [kg/h]
CO2 feed	1.00	30.00	101.30	300.00	13202.91
H2 feed	1.00	30.00	101.30	900.00	1814.40
dummy	0.00	448.67	3450.00	0.00	0.00
Gas	1.00	-130.00	3450.00	1431.95	6810.94
Liquid Product + CO2 + Water	0.00	-130.00	3450.00	767.60	23242.16
Only CO2	0.00	-10.00	3450.00	299.91	13189.43
Others	0.00	-218.33	3450.00	467.69	10052.73
Water Only	0.00	-225.29	3450.00	446.71	8047.59
Main Products	0.00	-55.00	3450.00	20.98	2005.15
Total CO2	0.00	-9.80	3450.00	300.48	13214.62
Raw Material	1.00	29.81	101.30	1200.00	15017.31
Reactor_out	1.00	350.00	3450.00	2199.55	30053.10
reactor_out_cooled	0.65	-130.00	3450.00	2199.55	30053.10
Others 2	1.00	-130.05	3450.00	1431.38	6785.74
CO2 2	1.00	0.03	3450.00	0.57	25.20
H2 only	1.00	-130.00	3450.00	1281.36	2583.21
CO only	1.00	-114.76	3450.00	150.02	4202.53
Raw Mat with recycle	1.00	98.47	3450.00	2403.83	30053.10
H2 to mix CO2	1.00	-130.00	3450.00	903.36	1821.17
H2 feed2Other	1.00	-130.00	3450.00	378.00	762.05
raw mat with recycle heated	1.00	350.00	3450.00	2403.83	30053.10
Main Recycle Stream	0.79	-83.89	3450.00	1203.83	15035.79
To recycle	1.00	-47.99	3450.00	1203.83	15035.79
main recy heated	1.00	-47.99	3450.00	1203.83	15035.79
Syngas	1.00	-128.80	3450.00	450.15	4807.59

H2 vent	1.00	-130.00	3450.00	77.87	156.98
H2 to CO	1.00	-130.00	3450.00	300.13	605.07
Raw_mat_comp1	1.00	389.14	1200.00	1200.00	15017.31
raw mat comp 2	1.00	242.49	3450.00	1200.00	15017.31
raw_mat_comp1_cool ed	1.00	90.00	1200.00	1200.00	15017.31
syngas_cooled	1.00	250.00	5000.00	1551.81	16576.56
Raw_Mat	1.00	-129.00	3450.00	450.00	4806.44
dummy	0.00	584.83	5000.00	0.00	0.00
Reactor_out_cooled	0.88	-55.00	300.00	1251.81	16576.41
To recy	1.00	-55.00	300.00	1101.81	11770.13
MeOH	0.00	-55.00	300.00	150.00	4806.29
recycle_main	1.00	-55.00	300.00	1101.81	11770.13
syngas_comp	1.00	-107.07	5000.00	450.00	4806.44
Reactor_Out	1.00	250.00	5000.00	1251.81	16576.41
reactor_out_decomp	1.00	76.79	300.00	1251.81	16576.41
Reactor_Out-2	1.00	300.00	5000.00	125.00	1655.25
reactor_out_decomp-2	1.00	76.79	300.00	125.00	1655.25
Feed to Reactor	1.00	188.88	5000.00	1551.81	16576.56
Recycle_main_comp	1.00	309.83	5000.00	1101.81	11770.13
Pre_decomp_heated	1.00	300.00	5000.00	1251.81	16576.41

Aspen HYSYS Simulation:

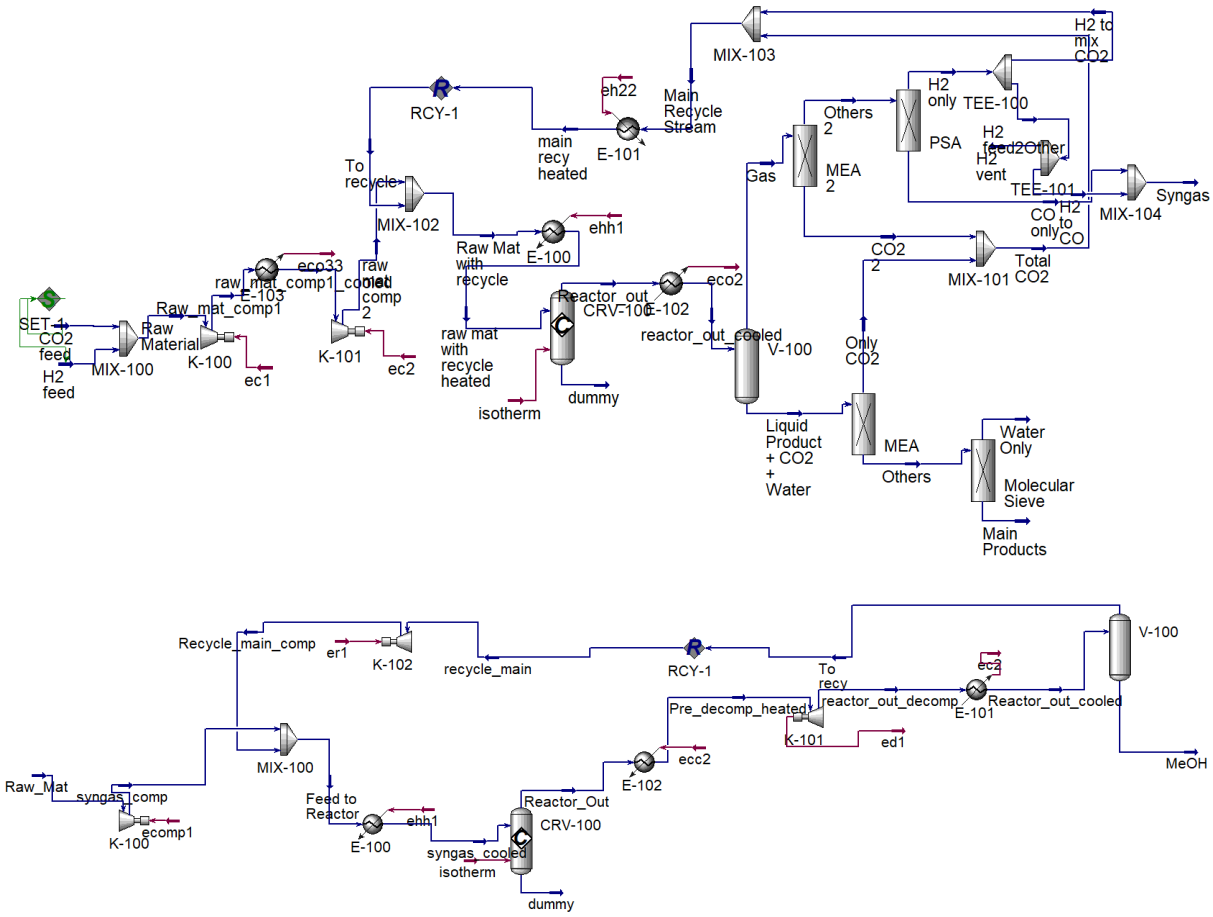

Fig. S14: Process flow diagram in Aspen HYSYS.

Table S9: Lang factors used in computing CAPEX[6,7]

Description	Lang Factor
Direct Costs (DC)	
Purchased equipment cost	1.00
Purchased equipment installation	0.47
Instrumentation and controls	0.36
Piping	0.68
Electrical system	0.11
Building (including services)	0.18
Yard improvements	0.10
Service facilities	0.70
Total direct costs	–
Indirect Costs (IC)	
Engineering and supervision	0.33
Construction expense	0.41
Legal expense	0.04
Contractor's fee	0.22
Contingency	0.44
Total indirect costs	–
Fixed Capital Investment (FCI)	**5.04**
Working Capital (WC)	**0.89**
CAPEX	**5.93**

Table S10: Methodology for computing OPEX[6,7]

Cost Category	Calculation Method
Variable Costs	
Operating Labor (OL)*	$\Sigma_i W^h (6.29 + 0.23 PU_i)^{0.5}$
Operating Supervision (OS)	0.15 of OL
Maintenance and Repairs (MR)	0.07 of FCI
Operating Supplies	0.15 of MR
Laboratory Charges	0.15 of OL
Royalties	0.04 of TPC
Fixed Costs	
Taxes	0.02 of FCI
Insurance	0.01 of FCI
Plant Overhead Costs	
General Expenses	0.6 of (OL + OS + MR)
Administrative	0.2 of (OL + OS + MR)
Distribution and Marketing	0.05 of TPC
Research and Development	0.05 of TPC

The cost analysis in this study was performed using Aspen Economic Analyzer. The purchase equipment costs were obtained directly from Aspen HYSYS, and the capital expenditure (CAPEX) was estimated using the cost correlations provided in Table S8. The operating expenditure (OPEX) was calculated following the methodology outlined in Table S9, where the total product cost (TPC) is defined as the sum of feed and utility costs. The utility costs are obtained from Aspen HYSYS.

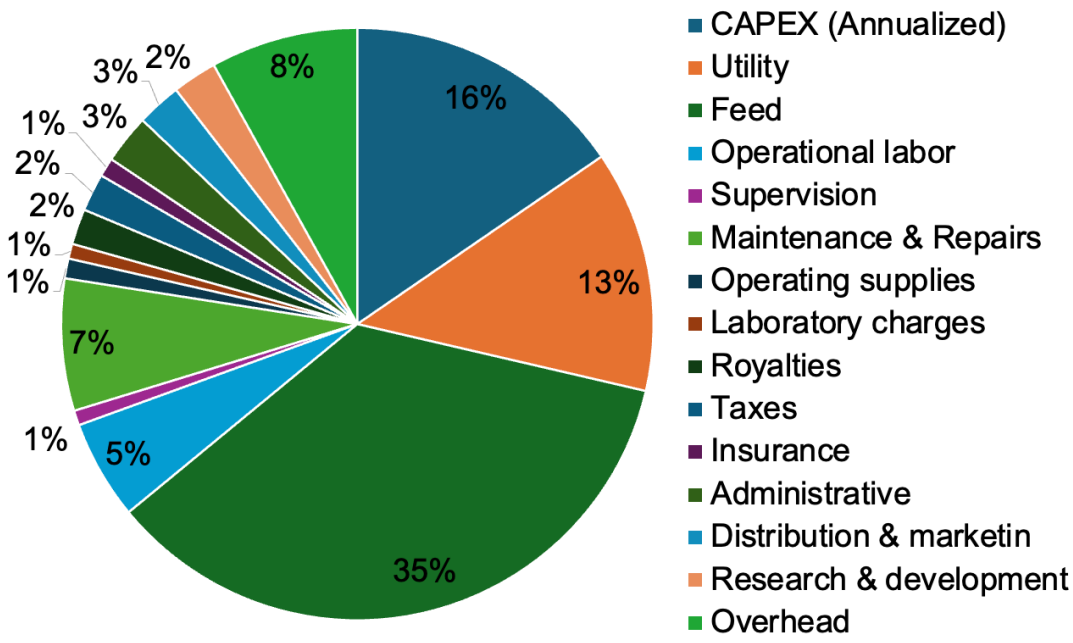

Fig. S15: Total production cost distribution.

Table S11: Price used for the process analysis.[40,41]

Chemical	Price
CO_2	2.2 $/ton
H_2	1.26 $/kg
Olefin	1 $/kg
Aromatics	1.2 $/kg
Ethylene and propylene	1 $/kg

T

Table S12. Data used for bubble plot in Fig. 5K.

Technology	Phi	Profit ($/$CO_2$ feed)	NCE (kg CO_2 emission/ kg product)
A	0.01	0.091684507	0.828032998
A	0.11045226	0.186899663	0.881221382
A	0.21090452	0.308733758	0.960131151
A	0.31135678	0.375662182	1.009805519
A	0.41180905	0.386361259	1.018262253
A	0.51226131	0.376017617	1.358474987
A	1.01452261	0.201264372	1.206126276
A	3.02356784	-0.116979274	1.002654824
A	5.03261307	-0.187331446	0.964659857
A	7.04165829	-0.216629484	0.949673028
B	0.01	0.0730342	1.56953591
B	0.11045226	0.168249356	1.670354451
B	0.21090452	0.290083451	1.819933479
B	0.31135678	0.357011875	1.914094452
B	0.41180905	0.367710953	1.930093083
B	0.51226131	0.357367311	2.263012465
B	1.01452261	0.182614065	2.002981515
B	3.02356784	-0.135629581	1.657534523
B	5.03261307	-0.205981753	1.594723306
B	7.04165829	-0.235279791	1.569947894
C	0.01	0.013974896	0.210978127
C	0.11045226	0.109190051	0.224530227
C	0.21090452	0.231024146	0.244631312
C	0.31135678	0.297952571	0.257285359
C	0.41180905	0.308651648	0.259465968
C	0.51226131	0.298308006	0.605747994
C	1.01452261	0.12355476	0.543008979
C	3.02356784	-0.194688886	0.457685006
C	5.03261307	-0.265041058	0.440341323
C	7.04165829	-0.294339095	0.433500238
D	0.01	0.006203934	-0.212490902
D	0.11045226	0.10141909	-0.226140174
D	0.21090452	0.223253185	-0.246397989
D	0.31135678	0.290181609	-0.259150045
D	0.41180905	0.300880687	-0.261276581
D	0.51226131	0.290537045	0.089170646
D	1.01452261	0.115783799	0.087928481
D	3.02356784	-0.202459847	0.08368611
D	5.03261307	-0.272812019	0.080514878
D	7.04165829	-0.302110057	0.07926401
E	0.01	-0.037313448	0.168631224
E	0.11045226	0.057901708	0.179463186
E	0.21090452	0.179735803	0.195528382
E	0.31135678	0.246664227	0.205641819
E	0.41180905	0.257363304	0.207391713
E	0.51226131	0.247019662	0.554090259
E	1.01452261	0.072266417	0.497500929
E	3.02356784	-0.245977229	0.420285116
E	5.03261307	-0.316329401	0.404358679
E	7.04165829	-0.345627439	0.398076615
F	0.01	-0.043530217	-0.222861572
F	0.11045226	0.051684939	-0.237177
F	0.21090452	0.173519034	-0.258423196
F	0.31135678	0.240447458	-0.271797443
F	0.41180905	0.251146535	-0.27402946
F	0.51226131	0.240802893	0.076519772
F	1.01452261	0.066049648	0.076783653
F	3.02356784	-0.252193998	0.074526954
F	5.03261307	-0.32254617	0.071702802
F	7.04165829	-0.351844208	0.070588837
G	0.01	-0.060626331	-0.091499751
G	0.11045226	0.034588824	-0.097377203
G	0.21090452	0.156422919	-0.106103903
G	0.31135678	0.223351344	-0.111597073

G	0.41180905	0.234050421	-0.112492996
G	0.51226131	0.223706779	0.236764174
G	1.01452261	0.048953533	0.217951481
G	3.02356784	-0.269290113	0.190542938
G	5.03261307	-0.339642285	0.183322434
G	7.04165829	-0.368940322	0.180474361
H	0.01	-0.09481856	0.04331896
H	0.11045226	0.000396595	0.046101537
H	0.21090452	0.12223069	0.050223793
H	0.31135678	0.189159115	0.052819097
H	0.41180905	0.199858192	0.053294428
H	0.51226131	0.18951455	0.401225534
H	1.01452261	0.014761304	0.362834251
H	3.02356784	-0.303482342	0.309611974
H	5.03261307	-0.373834514	0.297879425
H	7.04165829	-0.403132551	0.293251609
I	0.01	-0.236250053	-1.57623402
I	0.11045226	-0.141034898	-1.677482812
I	0.21090452	-0.019200803	-1.827712759
I	0.31135678	0.047727622	-1.922282837
I	0.41180905	0.058426699	-1.938280136
I	0.51226131	0.048083057	-1.574419262
I	1.01452261	-0.126670189	-1.377616469
I	3.02356784	-0.444913835	-1.120742985
I	5.03261307	-0.515266007	-1.078273142
I	7.04165829	-0.544564044	-1.061521232
J	0.01	-0.767783796	-0.250516692
J	0.11045226	-0.67256864	-0.266608537
J	0.21090452	-0.550734545	-0.290490416
J	0.31135678	-0.483806121	-0.305523837
J	0.41180905	-0.473107043	-0.308037136
J	0.51226131	-0.483450685	0.042784109
J	1.01452261	-0.658203931	0.04706411
J	3.02356784	-0.976447577	0.050102536
J	5.03261307	-1.046799749	0.048203932
J	7.04165829	-1.076097787	0.047455042
K	0.01	-0.934082364	-0.240146022
K	0.11045226	-0.838867209	-0.255571711
K	0.21090452	-0.717033113	-0.278465208
K	0.31135678	-0.650104689	-0.292876439
K	0.41180905	-0.639405612	-0.295284258
K	0.51226131	-0.649749254	0.055434983
K	1.01452261	-0.8245025	0.058208938
K	3.02356784	-1.142746145	0.059261693
K	5.03261307	-1.213098317	0.057016008
K	7.04165829	-1.242396355	0.056130215
L	0.01	-1.577517947	-0.125204429
L	0.11045226	-1.482302791	-0.133246888
L	0.21090452	-1.360468696	-0.145185827
L	0.31135678	-1.293540272	-0.152701115
L	0.41180905	-1.282841195	-0.153939852
L	0.51226131	-1.293184837	0.195648834
L	1.01452261	-1.467938082	0.181730788
L	3.02356784	-1.786181728	0.160775679
L	5.03261307	-1.8565339	0.154683186
L	7.04165829	-1.885831938	0.152280049

We are considering 12 different hydrogen production technology (the production cost of H_2 and associated CO_2 emission are mainly considered for each technology, please see Table S12 and S13 in the supplementary information). They are: A: Steam methane reforming (SMR), B: Coal gasification, C: Methane pyrolysis, D: Thermochemical water splitting (S-I) cycle, E: SMR with CCS, F: Thermochemical water splitting (Cu-Cl) cycle, G: Biomass gasification, H: Coal gasification with CCS, I: Biomass gasification with CCS, J: Electrolysis – nuclear, K: Electrolysis – wind, L: Electrolysis – solar.

Table S13: Cost of producing H_2 ($/kg) by different technologies.[43]

#	Technology	Cost ($/kg)
A	Steam methane reforming	1.26
B	Coal gasification	1.38
C	Methane pyrolysis	1.76
D	Thermochemical water splitting (S-I cycle)	1.81
E	SMR with carbon capture sequestration (CCS)	2.09
F	Thermochemical water splitting (Cu–Cl) cycle	2.13
G	Biomass gasification	2.24
H	Coal gasification with CCS	2.46
I	Biomass gasification with CCS	3.37
J	Electrolysis – nuclear	6.79
K	Electrolysis – wind	7.86
L	Electrolysis – solar	12.00

Table S14: CO_2 emissions associated with H_2 production (kg CO_2-eq/kg H_2).[43]

#	Technology	CO_2 emissions
A	Steam methane reforming	13.24
B	Coal gasification	21.82
C	Methane pyrolysis	6.10
D	Thermochemical water splitting (S-I cycle)	1.20
E	SMR with carbon capture sequestration (CCS)	5.61
F	Thermochemical water splitting (Cu–Cl) cycle	1.08
G	Biomass gasification	2.60
H	Coal gasification with CCS	4.16
I	Biomass gasification with CCS	-14.58
J	Electrolysis – nuclear	0.76
K	Electrolysis – wind	0.88
L	Electrolysis – solar	2.21

Separation of Hydrocarbons

The hydrocarbons were separated using two distillation columns. The first column separated ethene and propene on the top and the rest at the bottom. The bottom products of the first distillation column were sent to the second distillation column where olefins were collected at the top and aromatics at the bottom. For the first column the condenser and reboiler temperature were around 23^{o}C and 180^{o}C respectively. For the second column they were around 117^{o}C and 250^{o}C respectively. Both of the columns were operating at 1000 kPa. Shortcut distillation models were used initially to estimate the design parameters (e.g., tray number, reflux ratio, condenser/reboiler duties). These parameters are then supplied as initial guesses for the rigorous distillation columns. The target purity for all the products was >98%. The composition of hydrocarbons were different for different thiele modulus. When thiele modulus was below 0.2, only second distillation column was employed due not having enough ethene and propene in the hydrocarbon mixture for separation (<1%).

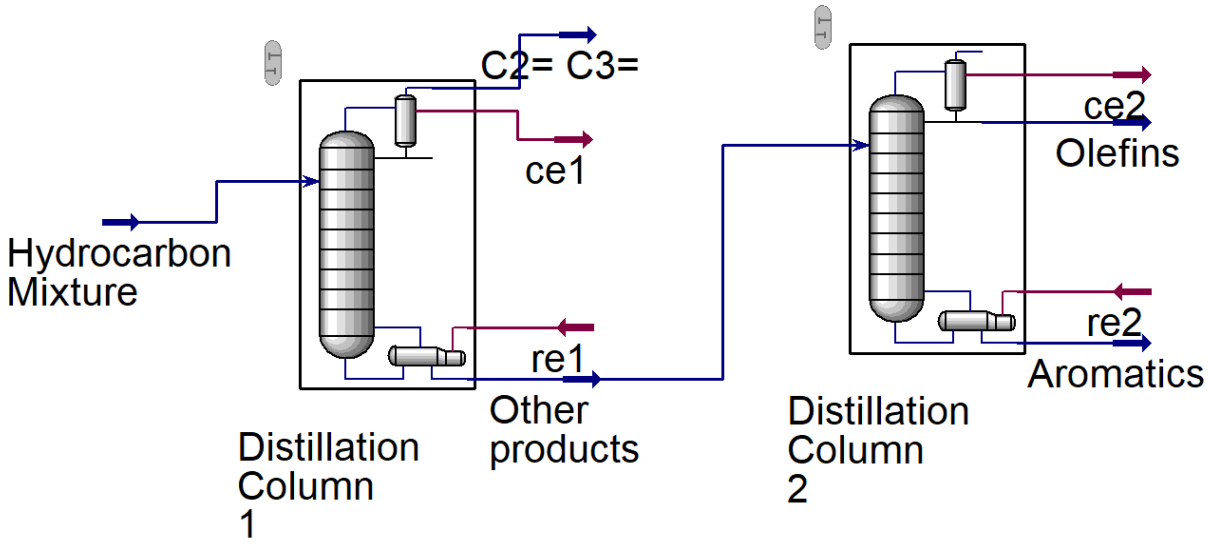

Fig. S16: Separation of hydrocarbons.

S18. DFT calculations

All zeolite calculations were carried out using VASP[42] on an orthorhombic cell (20.2 × 19.9 × 13.3 Å, α, β, γ = 90°) of ZSM-5 taken from International Zeolite Association (IZA) and comprising 96 silicon and 192 oxygen atoms with 12 distinct tetrahedral sites. We choose T7 as the location of Bronsted acid site per prior work;[43] an Al atom substitutes the Si atom and an additional H was added to O17 (per IZA naming convention) such that the H atom points along the straight channel, being hydrogen bonded to a nearby O.

Projected-Augmented-Wave (PAW) potentials with generalized gradient approximation (GGA) using the Perdew-Burke-Ernzerhof (PBE)[44] exchange correlational functional were used in all calculations along with a D2 dispersion correction because of lower errors when modeling small adsorbates in other zeolites.[45,46] A plane-wave energy cutoff of 400 eV was applied along with a cutoff of 10^{-4} eV for convergence of electronic relaxation. The ionic convergence was set to all forces on the system being less than 0.02 eV/A. Gaussian smearing of 0.1 eV was used and all energies were extrapolated to 0K. Only the Gamma point of the unit cell was sampled in view of the large cell size. Climbing image nudged elastic band (CI-NEB) calculations[47] with seven images were employed to locate the transition states; the convergence criterion was that the force on each image was less than 0.1 eV/A.

References

1 Brunauer, S., Emmett, P. H. & Teller, E. Adsorption of Gases in Multimolecular Layers. *Journal of the American Chemical Society* **60**, 309-319 (1938). https://doi.org:10.1021/ja01269a023

2 Anton Paar QuantaTec, I. in *autosorb iQ Gas Sorption System* (Graz, Austria, 2022).

3 Fogler, H. S. *Essentials of Chemical Reaction Engineering: Essenti Chemica Reactio Engi*. (Pearson Education, 2010).

4 Bird, R., Stewart, W. & Lightfoot, E. Other mechanisms for mass transport. *Transport Phenomena, John Wiley & Sons, Inc* (2007).

5 Davis, M. E. & Davis, R. J. *Fundamentals of chemical reaction engineering*. (Courier Corporation, 2012).

6 Fogler, H. S. Essentials of chemical reaction engineering. (2011).

7 Jiao, Y. *et al.* Creation of Al-enriched mesoporous ZSM-5 nanoboxes with high catalytic activity: converting tetrahedral extra-framework Al into framework sites by post treatment. *Angewandte Chemie International Edition* **59**, 19478-19486 (2020).

8 Fuller, E. N., Schettler, P. D. & Giddings, J. C. New method for prediction of binary gas-phase diffusion coefficients. *Industrial & Engineering Chemistry* **58**, 18-27 (1966).

9 Schechter, R. S. (ACS Publications, 1961).

10 Arena, F. *et al.* Effects of oxide carriers on surface functionality and process performance of the Cu–ZnO system in the synthesis of methanol via CO2 hydrogenation. *Journal of catalysis* **300**, 141-151 (2013).

11 Smith, J. M. (ACS Publications, 1950).

12 Li, Z. *et al.* Highly selective conversion of carbon dioxide to lower olefins. *Acs Catalysis* **7**, 8544-8548 (2017).

13 Gao, P. *et al.* Direct conversion of CO2 into liquid fuels with high selectivity over a bifunctional catalyst. *Nature chemistry* **9**, 1019-1024 (2017).

14 Numpilai, T., Wattanakit, C., Chareonpanich, M., Limtrakul, J. & Witoon, T. Optimization of synthesis condition for CO2 hydrogenation to light olefins over In2O3 admixed with SAPO-34. *Energy Conversion and Management* **180**, 511-523 (2019).

15 Tada, S. *et al.* Search for solid acid catalysts aiming at the development of bifunctional tandem catalysts for the one-pass synthesis of lower olefins via CO2 hydrogenation. *International Journal of Hydrogen Energy* **46**, 36721-36730 (2021).

16 Ramirez, A. *et al.* Multifunctional catalyst combination for the direct conversion of CO2 to propane. *Jacs Au* **1**, 1719-1732 (2021).

17 Wang, S. *et al.* Highly selective hydrogenation of CO2 to propane over GaZrO x/H-SSZ-13 composite. *Nature Catalysis* **5**, 1038-1050 (2022).

18 Guo, S. *et al.* Catalytic performance of various zinc-based binary metal oxides/H-RUB-13 for hydrogenation of CO2. *Industrial & Engineering Chemistry Research* **61**, 10409-10418 (2022).

19 Singh, G., Panda, S., Shrivastaw, V. K. & Bordoloi, A. Controlled acidity-mediated short-chain olefin synthesis over a Mn–Zn–Zr/Zn-SAPO-34 catalyst via CO 2 hydrogenation. *Chemical Communications* **61**, 4694-4697 (2025).

20 Li, Z. *et al.* Highly selective conversion of carbon dioxide to aromatics over tandem catalysts. *Joule* **3**, 570-583 (2019).

21 Zhou, C. *et al.* Highly active ZnO-ZrO2 aerogels integrated with H-ZSM-5 for aromatics synthesis from carbon dioxide. *ACs Catalysis* **10**, 302-310 (2019).

22 Ticali, P. *et al.* CO 2 hydrogenation to methanol and hydrocarbons over bifunctional Zn-doped ZrO 2/zeolite catalysts. *Catalysis Science & Technology* **11**, 1249-1268 (2021).

23 Wang, T. *et al.* ZnZrOx integrated with chain-like nanocrystal HZSM-5 as efficient catalysts for aromatics synthesis from CO2 hydrogenation. *Applied Catalysis B: Environmental* **286**, 119929 (2021).

24 Xin, Q. *et al.* Indium-promoted znZrOx/nano-ZSM-5 for efficient conversion of CO2 to aromatics with high selectivity. *Journal of Environmental Chemical Engineering* **10**, 108032 (2022).

25 Liu, B. *et al.* y In2O3-ZnZrO x/Hierarchical ZSM-5 Tandem Catalysts for CO2 Hydrogenation to Aromatics Rich in Tetramethylbenzene. *ACS Sustainable Chemistry & Engineering* **11**, 17340-17354 (2023).

26 Nezam, I. *et al.* Role of Catalyst Domain Size in the Hydrogenation of CO2 to Aromatics over ZnZrO x/ZSM-5 Catalysts. *The Journal of Physical Chemistry C* **127**, 6356-6370 (2023).

27 Liu, Z., Ni, Y., Sun, T., Zhu, W. & Liu, Z. Conversion of CO2 and H2 into propane over InZrOx and SSZ-13 composite catalyst. *Journal of Energy Chemistry* **54**, 111-117 (2021).

28 Di, W. *et al.* Modulating the Formation of Coke to Improve the Production of Light Olefins from CO2 Hydrogenation over In2O3 and SSZ-13 Catalysts. *Energy & Fuels* **37**, 17382-17398 (2023).

29 Chen, S. *et al.* Hydrogenation of CO2 to Light Olefins over ZnZrOx/SSZ-13. *Angewandte Chemie* **136**, e202316874 (2024).

30 Kuddusi, Y., Piveteau, L., Mensi, M., Cano-Blanco, D. C. & Züttel, A. Selective light olefin synthesis with high ethylene abundance via CO2 hydrogenation over (Ga-In) 2O3/SSZ-13 catalysts. *Journal of CO2 Utilization* **91**, 103001 (2025).

31 Wang, M. *et al.* Spinel nanostructures for the hydrogenation of CO2 to methanol and hydrocarbon chemicals. *Journal of the American Chemical Society* **146**, 14528-14538 (2024).

32 Cordero-Lanzac, T. *et al.* Transitioning from methanol to olefins (MTO) toward a tandem CO2 hydrogenation process: on the role and fate of heteroatoms (Mg, Si) in MAPO-18 zeotypes. *JACS Au* **4**, 744-759 (2024).

33 Phounglamcheik, A., Bäckebo, M., Robinson, R. & Umeki, K. The significance of intraparticle and interparticle diffusion during CO2 gasification of biomass char in a packed bed. *Fuel* **310**, 122302 (2022).

34 Xie, T., Ding, J., Shang, X., Zhang, X. & Zhong, Q. Effective synergies in indium oxide loaded with zirconia mixed with silicoaluminophosphate molecular sieve number 34 catalysts for carbon dioxide hydrogenation to lower olefins. *Journal of Colloid and Interface Science* **635**, 148-158 (2023).

35 Araujo, T. P. *et al.* Design of flame-made ZnZrOx catalysts for sustainable methanol synthesis from CO2. *Advanced Energy Materials* (2023).

36 Balasubramanian, V., Haque, N., Bhargava, S. K. & Parthasarathy, R. Techno-economic comparison of ammonia cracking and separation using metal membrane and pressure swing adsorption. *International Journal of Hydrogen Energy* **166**, 150904 (2025).

37 Nizami, M., Nugroho, R. I., Milati, K. H., Pratama, Y. W. & Purwanto, W. W. Process and levelized cost assessment of high CO2-content natural gas for LNG production using membrane and CFZ CO2 separation integrated with CO2 sequestration. *Sustainable Energy Technologies and Assessments* **49**, 101744 (2022).

38 Zhang, X., Yan, M., Feng, X., Wang, X. & Huang, W. Ethylene/propylene separation using mixed matrix membranes of poly (ether block amide)/nano-zeolite (NaY or NaA). *Korean Journal of Chemical Engineering* **38**, 576-586 (2021).

39 Prabowo, B. H., Nurdini, L. & Trilaksono, G. in *AIP Conference Proceedings.* (AIP Publishing).

40 Mangalindan, J. R., Mahnaz, F., Vito, J., Suphavilai, N. & Shetty, M. Tandem Cu/ZnO/ZrO2-SAPO-34 System for Dimethyl Ether Synthesis from CO2 and H2: Catalyst Optimization, Techno-Economic, and Carbon-Footprint Analyses. *ACS Engineering Au* (2025).

41 Parkinson, B., Balcombe, P., Speirs, J., Hawkes, A. & Hellgardt, K. Levelized cost of CO 2 mitigation from hydrogen production routes. *Energy & environmental science* **12**, 19-40 (2019).

42 Kresse, G. & Furthmüller, J. Efficient iterative schemes for ab initio total-energy calculations using a plane-wave basis set. *Physical review B* **54**, 11169 (1996).

43 Ghorbanpour, A., Rimer, J. D. & Grabow, L. C. Periodic, vdW-corrected density functional theory investigation of the effect of Al siting in H-ZSM-5 on chemisorption properties and site-specific acidity. *Catalysis Communications* **52**, 98-102 (2014).

44 Perdew, J. P., Burke, K. & Ernzerhof, M. Generalized gradient approximation made simple. *Physical review letters* **77**, 3865 (1996).

45 Zhang, Y. *et al.* An adsorption study of CH4 on ZSM-5, MOR, and ZSM-12 zeolites. *The Journal of Physical Chemistry C* **119**, 28970-28978 (2015).

46 Yeh, Y.-H., Rzepa, C., Rangarajan, S. & Gorte, R. J. Influence of brønsted-acid and cation-exchange sites on ethene adsorption in ZSM-5. *Microporous and Mesoporous Materials* **284**, 336-342 (2019).

47 Henkelman, G., Uberuaga, B. P. & Jónsson, H. A climbing image nudged elastic band method for finding saddle points and minimum energy paths. *The Journal of chemical physics* **113**, 9901-9904 (2000).